

PEP full public data release (DR1): PACS data

The PEP data reduction and extraction groups, with contributions by:
Stefano Berta, Benjamin Magnelli, Paola Popesso, Dieter Lutz, Francesca Pozzi,
Bruno Altieri, Hervé Aussel, Hoseong Hwang, Emeric Le Floc’h,
Georgios Magdis, Raanan Nordon, Albrecht Poglitsch, Laurie Riguccini,
Amelie Saintonge, Li Shao

March 1st, 2013

1 Introduction

The *PACS Evolutionary Probe* (PEP, Lutz et al. 2011, Prop. ID KPGT_dlutz.1) is a Herschel guaranteed time deep extragalactic survey, targeting six among the most popular “blank fields”, ten lensing clusters of galaxies and two $z \sim 1$ clusters at wavelengths of 160, 100, and partly $70\mu\text{m}$. SPIRE 250–500 μm coverage of these fields is available from the HerMES survey (Oliver et al. 2010a). In addition, deep SPIRE GOODS-N data are provided by the GOODS-Herschel program (Elbaz et al. 2011). This release note describes the content of the first, global, public data release of PEP data.

PACS observations of the GOODS-N and GOODS-S fields have been obtained not only by the PEP survey (total of 266 hours), but also by the open time key program *GOODS-Herschel* (Elbaz et al. 2011, total of 330 hours). For the two GOODS fields, the two teams thus jointly provide a combined public release, representing the deepest far-IR images and catalogs ever built. This combined release is described further in Magnelli et al. (2013).

2 Acknowledging PEP data from this release

If data from this release were useful for your research, please adhere to the following guidelines:

- Papers using PEP images or catalogs from this release for fields except GOODS-N/S should refer to the PEP survey description paper at an appropriate place, e.g. “Using data from the public data release of the PACS Evolutionary Probe PEP (Lutz et al. 2011)”.
- Papers using GOODS-S or GOODS-N images or catalogs from the reduction of the combined PEP/GOODS-Herschel data should cite these at an appropriate place, e.g., “Using combined Herschel-PACS data from the PEP (Lutz et al. 2011) and GOODS-Herschel (Elbaz et al. 2011) programs, as described in Magnelli et al. (2013)”.
- We also recall the usual Herschel conventions of placing a “Herschel is an ESA space observatory with science instruments provided by European-led Principal Investigator consortia and with important participation from NASA.” mandatory footnote on the frontpage, and citing the Pilbratt et al. (2010) Herschel seminal paper, as well as the applicable one(s) among the instrument seminal papers (Poglitsch et al. (2010); Griffin et al. (2010); de Graauw et al. (2010)).

3 Contents of the released package

PEP data releases are available at the PEP public website, direct link:

http://www.mpe.mpg.de/ir/Research/PEP/public_data_releases.php

High completeness blind catalogs of the PEP science demonstration phase fields were released in June 2011. Here, we describe the complete and full depth data release of images and catalogs for all fields.

PEP fields have been observed by PACS (Poglitsch et al. 2010), using the photometer scanmap mode at constant speed as described in (Lutz et al. 2011). We include observations of GOODS-S and Abell 2218 taken for Astronomical Observation Request (AOR) testing purposes during Herschel performance verification. Some of them were taken with 10 arcsec/s scanspeed. We appropriately underweight those data when averaging with data taken with default scanspeed 20 arcsec/s. For four lensing clusters, we have coadded PEP with data from the LoCuSS key program (Smith et al. 2010, KPOT_gsmith01_1), over the subarea covered by the PEP AORs.

We have observed the two high-redshift clusters also with SPIRE (Griffin et al. 2010). These are the only SPIRE data taken within PEP. A dedicated short release note describes them.

The total number of AORs employed for PACS observations of each blank field, and the corresponding total observing time, is summarized in Table 1. Details about the combined PEP and GOODS-Herschel dataset in the GOODS fields are given in Table 2, we sometimes refer to this dataset as ‘PGH’ for brevity. Observations of cluster fields are described in Table 3.

This release includes:

1. PACS maps including flux, error, and coverage
2. observed PSFs,
3. object masks used while building maps,
4. library (Vesta) PSFs manipulated so to match observed ones,
5. catalogs extracted blindly, down to 3σ significance,
6. cross-IDs between the PACS blind catalog and the $24\ \mu\text{m}$ catalog, based on maximum likelihood,
7. catalogs extracted using $24\ \mu\text{m}$ position priors, down to 3σ significance,
8. curves for completeness and fraction of spurious sources for the aforementioned catalogs,
9. residual maps.

4 General properties of released data

The released PACS maps were obtained through a rather standard data reduction based on the PACS pipeline (Wieprecht et al. 2009). Reduction was done within the HIPE environment in the Herschel Common Science System (HCSS), with the addition of PEP optimized procedures. We adopt the *high-pass filtering* plus direct map-making approach. *This approach is optimized for point source sensitivity and will remove large scale emission such as cirrus, faint anyway for cosmological fields which are selected for low galactic foreground.*

The reduction first proceeds on a per AOR level. First of all, the science-useful portions of each AOR are identified and distinguished from functional blocks, scans turn-arounds, and so on, on the basis of the velocity associated to each frame. Then bad pixels, saturated data, pixels affected by cross-talk contamination, etc. are flagged and no more used. Detector signals are converted into physical units, using the latest calibration files. Specifically for flux calibration, the maps in this release are based on v6 (blank fields) and v7 (clusters) of the photometer responsivity calibration file. PACS flux calibration assumes a flat $\nu F_\nu = \text{const}$ spectrum. Color corrections may be needed, but have not been applied to the released catalogs given their dependence on individual SEDs and redshifts.

After adding to the time-ordered data frames the instantaneous pointing obtained from the Herschel pointing product, we apply *re-centering* corrections. These are derived by comparing PACS maps obtained in a separate first processing of partial data-blocks to deep 24 μm catalogs with accurate astrometry. Short glitches in the detector time-lines caused by ionizing particle hits are flagged and interpolated with a multi-resolution median transform algorithm (Starck & Murtagh 1998).

The main source of noise in the PACS data is the so-called $1/f$ noise, with spectral density of the form $S(f) = 1/f^\alpha$, where f is frequency. The $1/f$ noise of the PACS photometer is roughly $\propto f^{-0.5}$ over the relevant frequencies.

In the specific case of deep extragalactic observations, the $1/f$ noise is removed with a high-pass filtering method. Specifically, the data timeline is filtered with a running box median filter of radius 12 or 20 samples at 70/100 μm and 160 μm , respectively. The median-filtered timeline is then subtracted from the original data. This choice of the high-pass filter radius allows us to subtract as much as possible $1/f$ noise, thus reducing the final map noise, without damaging the PACS PSF.

In order to avoid boosting of the median due to real sources on the frames, known objects are masked on the timeline and the corresponding readouts are excluded from the computation of the median. The mask is created on the basis of MIPS 24 μm catalogs and extends down to sources as faint as $S_{24} = 60 \mu\text{Jy}$. Any object (regardless of PACS detection) with $S_{24} < 60 \mu\text{Jy}$ was not masked. The mask is a circular patch at the position of each object, with a radius of 5 arcsec in the blue and green bands, and 7 arcsec in the red band for most fields (4 blue/green and 6 red for the very deep GOODS data). In a few cases with incomplete 24 μm coverage of the area observed by PACS, Herschel sources from a preliminary reduction were added to this list. Few known extended sources and bright “crowded” objects were manually flagged with larger patches. The final masks used are part of the release. Section 6 deals with the detailed effects of high-pass filtering, and describes simulations that have been run in order to quantify correction factors and their uncertainties (Popesso et al. 2012).

A single “sub-map” is created for each AOR, using the HCSS `photProject` algorithm, which is equivalent to the `drizzle` method (Fruchter & Hook 2002). Each individual AOR map is projected to the same world coordinate system (WCS). We use pixel scales of 1.2 arcsec and 2.4 arcsec for the 70, 100 μm and 160 μm maps, respectively. These scales significantly oversample the Point Spread Function (PSF) full width at half-maximum (FWHM, 6.7 arcsec and 11 arcsec at 100 μm and 160 μm), by factors of 5.6 and 4.6, respectively, which correspond to pixels twice smaller than the Nyquist

sampling. Given the high data redundancy in blank fields, PSF widths and noise correlation in the final map can be further reduced by choosing projection “drops” that are smaller than the physical PACS pixel size. The drop size is defined by the *pixfrac* parameter, which is the ratio between drop and input detector pixel size. We set *pixfrac* to 0.06, given the high data redundancy.

Finally, all sub-maps are combined together to produce our final data products, weights being given by the effective coverage of each pixel. The final error map is computed as the error of the weighted mean. Error maps have slightly larger values near the positions of PACS sources, probably due to small, residual jittering in the scan alignments. The final coverage map is the sum of all individual AOR coverages. Since we use a drizzle method, the coverage is obtained following Eq. 2 of Fruchter & Hook (2002). The coverage values are not the amount of time spent on sky pixel, but rather the sum of the fractional drop areas contributing to the sky pixel flux.

When dealing with PGH data, the PEP and GOODS-Herschel data have been combined also with 8 PACS Performance Verification (PV, see Table 2) AORs for GOODS-S, which were taken with preliminary observing modes. These 8 AORs are affected by a higher noise level per integration time, with respect to all other AORs. The main difference in this set of observations is in the scan speed of 10 arcsec/s instead of the 20 arcsec/s later adopted. We have taken into account this effect by properly weighting the PV AORs, when combining all sub-maps. The weights to be applied have been derived by combining 8 standard AORs and comparing the resulting noise properties to those of PV data alone. The resulting weight factors are 0.49 at 100 μm and 0.34 at 160 μm .

We defer to Lutz et al. (2011) for further details about data reduction and map making.

Field & Band	AORs	Obs. Time (s)
COSMOS 100	49	741634
COSMOS 160	49	741634
ECDFS 100	14	116452
ECDFS 160	14	116452
EGS 100	17	123210
EGS 160	17	123210
LH 100	20	128217
LH 160	20	128217
GOODS-N 100	75	–
GOODS-N 160	75	–
GOODS-S 070	96	–
GOODS-S 100	228	–
GOODS-S 160	324	–

Table 1: Total number of AORs and equivalent observing time for PEP blank fields.

4.1 Correction factors

We remind that, when extracting fluxes and flux uncertainties from PACS maps, one should keep in mind that a number of corrections might need to be applied. These corrections include aperture corrections due to the finite radius of the adopted PSFs, correlated noise corrections, and high-pass filtering effects.

Generally speaking, the absolute flux S of a given object is obtained from its extracted flux S' applying the equation:

Project/field	Band	GOODS-N	GOODS-S
PEP/GOODS	070 μm	–	96
<i>Total</i>	070 μm	–	96
PEP/GOODS	100 μm	22	108
PEP/ECDFS	100 μm	–	14
GOODS-H	100 μm	53	98
PACS PV	100 μm	–	8
<i>Total</i>	160 μm	75	228
PEP/GOODS	160 μm	22	204
PEP/ECDFS	160 μm	–	14
GOODS-H	160 μm	53	98
PACS PV	160 μm	–	8
<i>Total</i>	160 μm	75	324

Remember that PEP and GOODS-H AORs have different duration and for GOODS-S also cover different areas.

Table 2: PACS observations of the GOODS fields: combining PEP, GOODS-Herschel and PV data. This tables summarizes the number of AORs observed per band and project.

$$S(\lambda) = S'(\lambda) \times a(\lambda) \times g(\lambda) \quad (1)$$

where a is the aperture correction and g is due to the high-pass filtering losses for the specific filtering and masking strategy used here. Both factors depend on wavelength.

Similarly, the flux uncertainty E is obtained from the extracted uncertainty E' following the equation:

$$E = E' \times a(\lambda) \times g(\lambda) \times f(\lambda) \quad (2)$$

where here f represents a correction due to the correlation of noise in adjacent pixels.

All corrections a , g , f are already included in the catalogs provided, but they are not included in maps. Hence if one needs to extract a flux, e.g. following a stacking analysis, one needs to keep in mind these corrections.

Tables 4 and 5 summarize the most relevant information for this data release for blank and cluster fields, respectively. Details about the meaning of each term in the equations and in the Tables are given in the following Sections.

4.2 Released maps

Maps are presented in two different fits formats:

- data cubes directly reflecting the HIPE simpleImage: extension [1] is the science map; extension [2] is the error map; extension [3] is the coverage map; extension [4] contains the data processing history. Note that the HIPE history includes not only the direct reduction path, but also elements of other products used.
- individual science map, error and coverage maps, to be used with software not able to deal with datacubes.

Labels “blue”, “green” and “red” refer to the 70 μm , 100 μm , and 160 μm bands, respectively.

Field & Band	AORs	Obs. Time (s)
A1689 100	6(+2)	30816
A1689 160	6(+2)	30816
A1835 100	2(+2)	18840
A1835 160	2(+2)	18840
A2218 100	8(+2)	57784
A2218 160	8(+2)	57784
A2219 100	2(+2)	18840
A2219 160	2(+2)	18840
A2390 100	2(+2)	18840
A2390 160	2(+2)	18840
A370 100	2	18840
A370 160	2	18840
CL0024 100	2	22098
CL0024 160	2	22098
MS0451 100	2	18840
MS0451 160	2	18840
MS1054 100	6	17259
MS1054 160	6	17259
MS1358 100	2	18840
MS1358 160	2	18840
RXJ0152 100	6	17259
RXJ0152 160	6	17259
RXJ13475 100	2	18840
RXJ13475 160	2	18840

Table 3: Total number of AORs and equivalent observing time for PEP cluster fields. In parenthesis the number of AORs from KPOT_gmsith01_1 is reported; observing times are computed on PEP and PV AORs only, because others only partially overlap to PEP.

5 Observed PSFs

At the resolution of Herschel, most of the objects detected in deep fields are point sources. Therefore photometric catalogs have been extracted through a PSF-fitting approach.

Point Spread Functions (PSFs) were directly derived from the science maps during the blind source extraction process with the code Starfinder (Diolaiti et al. 2000a,b). A number of pointlike bright sources, as much isolated as possible, were stacked and then normalized to a unit total flux. Because of limitations in the signal-to-noise (S/N) ratio, these empirical PSFs have a finite size. Moreover they have been cut to small pixel radii (typically 6 and 5 pixels in the blue/green and red bands, respectively), in order to minimize the influence of filtering effects on the wings of the observed point-like profile.

Independent observations of very bright objects, such as the asteroid Vesta, have provided a measure of the in-flight PSF for our observing mode (scan map with speed 20"/s). Aperture corrections can be estimated from these “Vesta PSFs” (see also the PSF note PICC-ME-TN-033 v2.0) and the calibration Energy Enclosed Fraction (EEF) curves, by adapting them to the sky orientation and the width of PEP observed PSFs, and finally simply accounting for the limited radius adopted in during source extraction.

Field & band & latest internal version	Pixel scale	PSF radius	a	g	f
PEP COSMOS 100 μ m v. 3.0	1.2 "/pix	7.2"	1/0.667	1.12	1.35
PEP COSMOS 160 μ m v. 3.0	2.4 "/pix	12"	1/0.677	1.11	1.57
PEP ECDFS 100 μ m v. 2.0	1.2 "/pix	7.2"	1/0.673	1.12	1.35
PEP ECDFS 160 μ m v. 2.0	2.4 "/pix	12"	1/0.683	1.11	1.57
PEP EGS 100 μ m v. 2.0	1.2 "/pix	7.2"	1/0.666	1.12	1.35
PEP EGS 160 μ m v. 2.0	2.4 "/pix	12"	1/0.681	1.11	1.57
PEP LH 100 μ m v. 2.0	1.2 "/pix	7.2"	1/0.674	1.12	1.35
PEP LH 160 μ m v. 2.0	2.4 "/pix	12"	1/0.675	1.11	1.57
PGH GOODS-N 100 μ m v. 1.0	1.2 "/pix	7.2"	1/0.664	1.12	1.36
PGH GOODS-N 160 μ m v. 1.0	2.4 "/pix	12"	1/0.682	1.11	1.54
PGH GOODS-S 070 μ m v. 1.0	1.2 "/pix	9.6"	1/0.778	1.13	1.32
PGH GOODS-S 100 μ m v. 1.0	1.2 "/pix	7.2"	1/0.670	1.12	1.35
PGH GOODS-S 160 μ m v. 1.0	2.4 "/pix	12"	1/0.688	1.11	1.57

Table 4: Summary of relevant information for the latest PEP data releases, obtained with consistent reductions setups. Aperture corrections extend to a 1000 arcsec radius. We stress that these values hold only for source extractions performed on the released PEP and PGH maps, using the provided observed PSFs, cut at the radii quoted in Table 6.

Field & band & latest internal version	Pixel scale	PSF radius	a	g	f
PEP A1689 100 μ m v. 2.0	1.2 "/pix	7.2"	1/0.671	1.12	1.35
PEP A1689 160 μ m v. 2.0	2.4 "/pix	12"	1/0.687	1.11	1.57
PEP A1835 100 μ m v. 2.0	1.2 "/pix	7.2"	1/0.673	1.12	1.35
PEP A1835 160 μ m v. 2.0	2.4 "/pix	12"	1/0.682	1.11	1.57
PEP A2218 100 μ m v. 2.0	1.2 "/pix	7.2"	1/0.670	1.12	1.35
PEP A2218 160 μ m v. 2.0	2.4 "/pix	12"	1/0.681	1.11	1.57
PEP A2219 100 μ m v. 2.0	1.2 "/pix	7.2"	1/0.682	1.12	1.35
PEP A2219 160 μ m v. 2.0	2.4 "/pix	12"	1/0.682	1.11	1.57
PEP A2390 100 μ m v. 2.0	1.2 "/pix	7.2"	1/0.682	1.12	1.35
PEP A2390 160 μ m v. 2.0	2.4 "/pix	12"	1/0.682	1.11	1.57
PEP A370 100 μ m v. 2.0	1.2 "/pix	7.2"	1/0.681	1.12	1.35
PEP A370 160 μ m v. 2.0	2.4 "/pix	12"	1/0.680	1.11	1.57
PEP CL0024 100 μ m v. 2.0	1.2 "/pix	7.2"	1/0.674	1.12	1.35
PEP CL0024 160 μ m v. 2.0	2.4 "/pix	12"	1/0.682	1.11	1.57
PEP MS0451 100 μ m v. 2.0	1.2 "/pix	7.2"	1/0.677	1.12	1.35
PEP MS0451 160 μ m v. 2.0	2.4 "/pix	12"	1/0.675	1.11	1.57
PEP MS1054 100 μ m v. 2.0	1.2 "/pix	7.2"	1/0.672	1.12	1.35
PEP MS1054 160 μ m v. 2.0	2.4 "/pix	12"	1/0.687	1.11	1.57
PEP MS1358 100 μ m v. 2.0	1.2 "/pix	7.2"	1/0.672	1.12	1.35
PEP MS1358 160 μ m v. 2.0	2.4 "/pix	12"	1/0.681	1.11	1.57
PEP RXJ0152 100 μ m v. 2.0	1.2 "/pix	7.2"	1/0.674	1.12	1.35
PEP RXJ0152 160 μ m v. 2.0	2.4 "/pix	12"	1/0.683	1.11	1.57
PEP RXJ13475 100 μ m v. 2.0	1.2 "/pix	7.2"	1/0.670	1.12	1.35
PEP RXJ13475 160 μ m v. 2.0	2.4 "/pix	12"	1/0.679	1.11	1.57

Table 5: Same as Table 4, but for cluster fields.

Tables 6 and 7 list the aperture corrections needed to transform the fluxes extracted adopting the observed PSFs into total fluxes extended to a 1000 arcsec radius. Note that using Vesta aperture corrections as directly derived from the provided manipulated Vesta frames produces correction up to 60 arcsec radii; the factors needed to extend to 1000 arcsec are: 1/0.930, 1/0.919, and 1/0.908 in blue, green and red, respectively. See in this regard the note on PACS photometer point source flux

calibration (PICC-ME-TN-037, version 1.0), which should also be consulted when applying other approaches such as aperture photometry. Both notes are available on the PACS calibration wiki <http://herschel.esac.esa.int/twiki/bin/view/Public/PacsCalibrationWeb>.

Catalogs were extracted cutting PSFs to a small pixel radius, in order to minimize filtering effects on the wings of bright sources. **These aperture corrections are already included in the released catalogs.**

Field	band	radius	Included flux
PEP COSMOS	green	6 pix	0.667
PEP COSMOS	red	5 pix	0.677
PEP ECDFS	green	6 pix	0.673
PEP ECDFS	red	5 pix	0.683
PEP EGS	green	6 pix	0.666
PEP EGS	red	5 pix	0.681
PEP LH	green	6 pix	0.674
PEP LH	red	5 pix	0.675
PGH GOODS-N	green	6 pix	0.664
PGH GOODS-N	red	5 pix	0.682
PGH GOODS-N	blue	8 pix	0.778
PGH GOODS-N	green	6 pix	0.670
PGH GOODS-N	red	5 pix	0.688

Table 6: Fraction of flux included in extraction radii, computed on manipulated library Vesta PSF and extended to a radius of 1000 arcsec.

6 Effect of high-pass filtering

Simulations performed to study the effect of the high-pass filter on PSF’s shape and extracted fluxes showed that — even when masking sources — there does exist a flux loss, of order 10% and 20% for parameters as used here.

The same simulations showed also that if the sources are not masked at all, or — alternatively — if they are all masked in the same way, such flux loss does not depend on flux, in the flux regime covered by deep surveys.

Masks based on the S/N ratio (like those adopted in previous internal PEP data releases) — instead — introduce a flux dependency, because the brighter the flux, the larger the region masked and, thus, the smaller the flux loss for point-sources. In this case the total flux of the bright sources is almost completely retrieved, while there is a larger flux loss at the faint end. This kind of strategy does not allow to easily apply a high-pass filtering correction to the extracted fluxes, because such a correction is flux-dependent.

Let’s now focus on the PEP case, adopting fixed-radius patches as masks. Given the high-pass filter width used for PEP, we performed dedicated simulations by adding artificial sources to a real PACS time-line made of spatially- and flux-calibrated *frames*. The artificial objects were added by back-projecting the *library Vesta* PSF and by taking into account the quantization of the PACS signal. Each simulation was performed by adding 60 artificial sources with the same flux in relatively isolated regions. The original time-lines (without any object added) were reduced in parallel with the

Field	band	radius	Included flux
PEP A1689	green	6 pix	0.671
PEP A1689	red	5 pix	0.687
PEP A1835	green	6 pix	0.673
PEP A1835	red	5 pix	0.682
PEP A2218	green	6 pix	0.670
PEP A2218	red	5 pix	0.681
PEP A2219	green	6 pix	0.682
PEP A2219	red	5 pix	0.682
PEP A2390	green	6 pix	0.682
PEP A2390	red	5 pix	0.682
PEP A370	green	6 pix	0.681
PEP A370	red	5 pix	0.680
PEP CL0024	green	6 pix	0.674
PEP CL0024	red	5 pix	0.682
PEP MS0451	green	6 pix	0.677
PEP MS0451	red	5 pix	0.675
PEP MS1054	green	6 pix	0.672
PEP MS1054	red	5 pix	0.687
PEP MS1358	green	6 pix	0.672
PEP MS1358	red	5 pix	0.681
PEP RXJ0152	green	6 pix	0.674
PEP RXJ0152	red	5 pix	0.683
PEP RXJ13475	green	6 pix	0.670
PEP RXJ13475	red	5 pix	0.679

Table 7: Fraction of flux included in extraction radii, computed on manipulated library Vesta PSF and extended to a radius of 1000 arcsec, for cluster fields.

same data reduction used for the simulated time-lines and for the real PEP released maps. In this way, it is possible to subtract the original map from the altered map and get rid of any background and noise. The result is a “residual” map containing only artificial sources, without noise. Hence we can now easily isolate the effect of high-pass filtering and avoid any uncertainties due to background subtraction. For more details about these simulations, we defer to Popesso et al. (2012).

The estimation of flux losses was performed in two ways:

- through aperture photometry with radii ranging from 2-4 to 22 arcsec on the “residual” map. The flux loss is estimated by comparing the curve of growth of the PSF obtained from the residual map with the back-projected PSF at the same flux and without high-pass filtering effect.
- through blind and priors source extraction from the altered map, adopting the same codes and setups used for the real PEP map.

Given the extraction aperture, the flux losses estimated in the two ways are consistent to each other.

The percentage of flux lost due to the high-pass filtering effect, is therefore 13%, 12% and 11% in the blue, green and red bands, respectively. **These values hold for maps and catalogs**

obtained with the setup (data reduction and extraction) adopted here for PEP (see Sections above), and in principle for masked sources only. For unmasked sources, a larger correction factor should be applied; simulations suggest that this could be of order 20% (see Popesso et al. 2012) However, in practice, the measured fluxes for unmasked sources have quite a very low S/N ratio, and therefore the missing $\sim 8\%$ correction is irrelevant with respect to the actual flux relative uncertainty. For this reason, a uniform correction of the high-pass filtering effect has been applied, regardless of whether the sources were masked or not during filtering.

These correction factors have been already applied to the released catalogs, but not to maps.

7 Correlated noise

The correlation maps describe the effect of correlated noise in a given pixel, coming from projections, drizzling, resampling, stacking and $1/f$ noise. These maps were produced again from the various independent maps for each field as also described in Lutz et al. (2011) and represent the correlation between two pixels according to their relative position in the map and averaged over a large sample number of locations in the map. The values in the correlation map are the correlation with the central pixel, which is assumed to be similar for every pair of science map pixels with the same Δx , Δy .

This correlation needs to be taken into account when integrating the noise using the PSF and error maps. The correlation map gives correlation factors to be used in the computation of the actual noise/error values to be associated to the extracted fluxes. The correlated error propagation for a weighted sum $f(x_1..x_n) = \sum_i^n a_i * x_i$, with correlations $\rho(i, j)$:

$$\sigma_f^2 = \sum_{i,j}^n a_i \sigma_i \cdot a_j \sigma_j \cdot \rho(i, j) \quad (3)$$

If the individual pixel errors are uniform, they can be taken out of the sum:

$$\sigma_f = \sigma_{pix} \sqrt{\sum_{i,j}^n a_i a_j \rho(i, j)} \quad (4)$$

In the case of non-correlated errors we set $\rho = 1$ for $i = j$ and $\rho = 0$ for $i \neq j$. The ratio $f = \sigma_{f,corr} / \sigma_{f,nocorr}$ between errors with and without taking correlations into account, or the *correction factor* is just a function of the weights a_i (the PSF) and the correlations $\rho(i, j)$ which are read from the correlation map and is independent of the pixel noise. This was tested across the map and even in areas near the edges of the map, the assumption of uniform errors leads to an error in the correction factor of less than 2%. Similarly, very similar values are found in different fields, therefore the same values of f are adopted in all cases, with the exception of PGH data for which slightly different f 's were adopted (see Table 4). For the PSF used in flux extraction the correction factors are:

$$\begin{aligned} f_{green} &= 1.35 \\ f_{red} &= 1.57 \end{aligned}$$

These correction factors are already included in the released catalogs, but are not factored into the error map, since they depend on the PSFs.

8 Blind catalogs

We used the Starfinder IDL code (Diolaiti et al. 2000a,b) to blindly extract the PACS catalogs, by means of PSF-fitting. We adopted the “direct” noise maps and extracted PSFs directly from the observed maps (see Section 5).

The released catalogs include all sources above a S/N threshold of 3σ , derived directly from the measured fluxes and flux uncertainties.

It is important to mention that the *direct* error map does not take into account the effects of correlated noise and therefore the output errors on fluxes have been multiplied by the correction factors described in Section 7. **This correction is already included in the released catalogs.**

Users should keep in mind that this error estimate does not take into account confusion noise. We recommend to use any flux below 0.6 mJy in the green band and below 2.0 mJy in the red band with care.

Tables 8 and 9 summarize the main properties of the extracted catalogs of blank and cluster fields, respectively.

8.1 Simulations

In order to quantify the detection rate (aka in-completeness) and the fraction of spurious detections in the PACS catalogs, we performed extensive Monte-Carlo simulations. Artificial sources were added to our images, following a flux distribution that approximately matches the measured far-IR number counts (Berta et al. 2010, 2011; Oliver et al. 2010b). The original statistics of images (e.g. crowding properties), have been preserved by adding only a small number of artificial objects at a time, and producing many simulated images — with sources added at different positions — until a total of 10000 artificial sources was reached.

Source extraction on these simulated frames was then performed with the same Starfinder configuration used for real objects. The three main quantities extracted from these simulations are photometric accuracy, completeness, and fraction of spurious sources (i.e. contamination) of our catalogs, as a function of flux density. Completeness is defined as the fraction of simulated sources extracted with a flux accuracy better than 50%. Contamination is defined as the fraction of simulated sources introduced with $S/N < 2$, but extracted with $S/N \geq 3$.

Figure 1 show the results of this analysis in the PGH GOODS-N field, as an example, and Table 8 includes the completeness and spurious fraction values at the 3σ and 5σ levels for all blank fields. Results for cluster fields are summarized in Table 9.

Despite fine-tuning, Starfinder tends to overestimate the flux of sources at the faintest flux levels. **A correction of this effect has already been applied to the released catalogs**, using the functions derived from simulations. Correction curves are provided in the released data package, in case users would like to un-correct fluxes. Curves of the completeness and the fraction of spurious sources as a function of flux are included as well.

Note that — given the inhomogeneity of GOODS-S 100 and 160 μm maps — GOODS-S simulations refer only to the central, deepest area.

8.2 Extended/bright sources

Some of the brightest objects in the PACS blind catalog (with fluxes of the order of 100 mJy) seem to be extended even on PACS images.

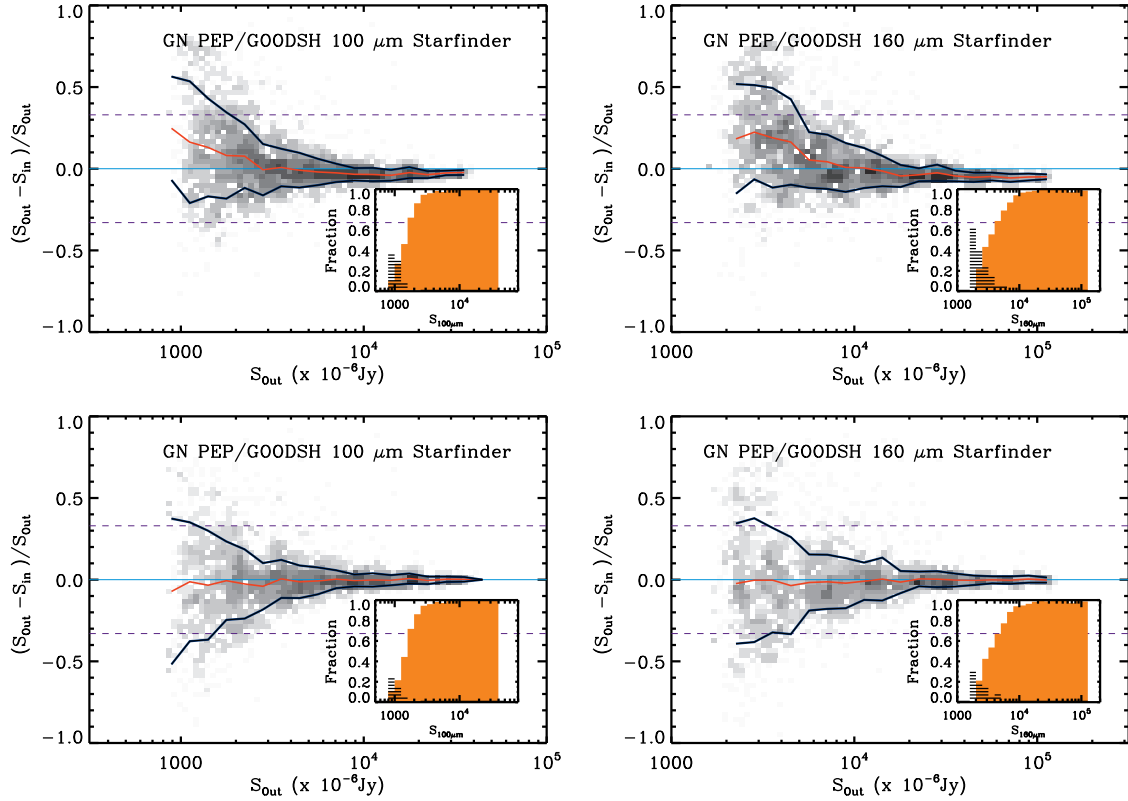


Figure 1: Results of “simulations” for blind extraction in PGH GOODS-N, before (*top*) and after (*bottom*) correcting flux trends. Comparison of input and output fluxes: red lines represent the average photometric accuracy, blue lines set the standard deviation observed in each flux bin (after 3σ clipping). Orange histograms represent the detection rate (or completeness) computed on the artificial injected sources. Completeness is defined as the fraction of sources that have been detected with a photometric accuracy of at least 50% (Papovich et al. 2004). Black hashed histograms show the fraction of spurious sources, defined as sources extracted above 3σ with an input flux lower than $3\sigma(\text{Image})$. The files corresponding to these diagrams, and included in this release are named: *pgh_GOODSN_100um_blind_Err_Compl_Contam.DR1.dat* (top left), *pgh_GOODSN_160um_blind_Err_Compl_Contam.DR1.dat* (top right), *pgh_GOODSN_100um_blind_Err_Compl_Contam.no_trend.DR1.dat* (bottom left), *pgh_GOODSN_160um_blind_Err_Compl_Contam.no_trend.DR1.dat* (bottom left).

Field & band	S(1σ) mJy	Num. $S/N \geq 3$	Num. $S/N \geq 5$	Completeness 3σ	f(spur) 3σ	Completeness 5σ	f(spur) 5σ	S(80%) mJy
COSMOS 100	1.50	7443	3398	0.10	0.24	0.66	0.06	8.68
COSMOS 160	3.27	7047	2581	0.15	0.25	0.65	0.09	20.33
ECDFS 100	1.25	1188	471	0.21	0.23	0.69	0.03	7.20
ECDFS 160	2.61	969	356	0.19	0.47	0.72	0.14	15.00
EGS 100	1.16	1249	559	0.19	0.19	0.67	0.03	6.53
EGS 160	2.46	940	976	0.20	0.38	0.69	0.13	14.27
LH 100	1.24	973	387	0.23	0.31	0.76	0.04	6.50
LH 160	2.92	819	279	0.23	0.43	0.68	0.11	17.90
PGH GN 100	0.31	1040	718	0.13	0.37	0.56	0.07	2.04
PGH GN 160	0.69	1055	623	0.16	0.48	0.53	0.17	5.88
PGH GS 070	0.27	468	226	0.19	0.19	0.72	0.11	1.51
PGH GS 100	0.17	1189	825	0.21	0.42	0.74	0.09	1.02
PGH GS 160	0.42	1240	832	0.15	0.47	0.45	0.08	4.89

Table 8: Statistics of blind catalogs for blank fields, within the trimmed areas. The 1σ flux level has been computed from random extractions on residual maps (see Section 10.2). On the other hand, the catalog has been cut at 3σ and 5σ on the basis of S/N simply computed as Flux/Error for each individual source. The completeness and fraction of spurious sources at 3σ and 5σ , as well as the 80% completeness level (last column), were obtained by interpolating the results of simulations before correcting flux trends. Corresponding values for catalogs including flux trends corrections can be computed from the files included in this release.

Field & band	S(1σ) mJy	Num. $S/N \geq 3$	Num. $S/N \geq 5$	Completeness 3σ	f(spur) 3σ	Completeness 5σ	f(spur) 5σ	S(80%) mJy
PEP A1689 100	0.57	183	104	0.20	0.56	0.68	0.12	3.56
PEP A1689 160	1.38	151	87	0.30	0.64	0.66	0.21	8.37
PEP A1835 100	0.89	111	55	0.27	0.25	0.76	0.07	4.82
PEP A1835 160	2.10	85	44	0.39	0.39	0.75	0.09	11.65
PEP A2218 100	0.71	165	93	0.15	0.40	0.47	0.18	7.77
PEP A2218 160	1.83	134	82	0.37	0.43	0.68	0.12	11.44
PEP A2219 100	0.83	114	55	0.24	0.31	0.72	0.05	4.45
PEP A2219 160	1.98	104	39	0.34	0.37	0.72	0.06	11.13
PEP A2390 100	0.91	130	87	0.19	0.22	0.59	0.02	6.35
PEP A2390 160	2.54	114	69	0.42	0.22	0.76	0.05	13.41
PEP A370 100	0.90	113	63	0.16	0.21	0.61	0.05	5.95
PEP A370 160	2.28	114	57	0.31	0.26	0.74	0.05	13.50
PEP CL0024 100	0.97	129	79	0.14	0.24	0.51	0.04	7.75
PEP CL0024 160	2.27	142	71	0.22	0.38	0.65	0.07	15.87
PEP MS0451 100	0.86	97	51	0.17	0.31	0.55	0.07	5.69
PEP MS0451 160	2.24	90	42	0.30	0.36	0.71	0.06	14.20
PEP MS1054 100	1.10	148	82	0.10	0.17	0.47	0.04	8.55
PEP MS1054 160	2.57	151	75	0.28	0.26	0.67	0.08	16.25
PEP MS1358 100	0.86	88	53	0.16	0.29	0.54	0.07	5.89
PEP MS1358 160	2.12	93	48	0.26	0.29	0.67	0.10	13.23
PEP RXJ0152 100	1.14	114	55	0.10	0.25	0.47	0.05	8.79
PEP RXJ0152 160	2.55	137	45	0.17	0.26	0.63	0.07	17.36
PEP RXJ13475 100	0.89	76	42	0.15	0.27	0.57	0.05	6.28
PEP RXJ13475 160	2.17	88	31	0.35	0.31	0.77	0.07	11.50

Table 9: Same as Table 8, but for cluster fields.

Since Starfinder performs PSF-fitting, it cannot properly handle extended sources. As a consequence, these objects have been split into sub-components during the blind extraction. This leads to erroneous flux estimates, erroneous number counts at the bright end, contamination of counts at intermediate fluxes by the sub-components, and so on.

We have decided to fix this problem by running SExtractor (Bertin & Arnouts 1996) on PACS images and go through the following procedure:

1. use SExtractor to extract new blind catalogs from the PACS maps. We use Kron elliptical apertures defined with a k scaling factor of 3.0 (instead of the default 2.5);
2. select the sources that are extended and might be affected by Starfinder problems. Do this using the geometrical parameters output of SExtractor;
3. visually check all candidates, in order to avoid to include real heavily blended sources, instead of extended/bright objects;
4. seek for sources extracted by Starfinder, at the position of the extended sources newly identified with SExtractor. Seek for all sources lying within the pixels covered by the given extended source (use SExtractor output geometrical parameters);
5. erase the sources selected above and inject the new extended objects in the final PACS blind catalogs:
 - if a given SExtractor’s extended source has only one matched source in the Starfinder catalog (or less), then keep the Starfinder entry without any modification;
 - if a given SExtractor’s extended source is matched to at least 2 sources in the Starfinder catalog, then erase all Starfinder’s sources affected and replace them with the given SExtractor’s source.

We have identified potentially affected sources using the SExtractor’s catalogs and testing dependences among geometrical parameters, fluxes, and SExtractor’s flags. The best way to identify these objects turned out to be by exploiting the *isophotal area vs. flux* space. Note that this method is totally empirical, and there might exist good alternatives. All sources selected in this way as being potentially contaminated, need then to be visually checked, as mentioned above. Figure 2 the selection adopted in COSMOS, as an example. The equations describing the adopted criteria (red lines) can be written as:

$$\begin{aligned} area &> A \text{ [pix]} \\ \log(area) &> a * \log(flux(\text{ap } 3, [\text{Jy}])) + b \end{aligned} \tag{5}$$

where “aperture 3” has a diameter of 15 pixels, and was defined as a good compromise to isolate these objects over the global population. Adopting a different aperture will lead to different slopes and normalizations in the equations listed above. The adopted values of A , a and b for all fields are listed in Tabs. 10 and 11.

The selection was verified by hand, by overplotting source positions (both Starfinder and SExtractor) on PACS maps (e.g. using DS9). In this way we could optimize the above selection criteria. We have attempted to lower the area threshold and modify the slopes/normalizations of the flux dependences, but no additional bright/extended sources split into sub-components were included.

As a by-product of this analysis and of visual checking, it turned out that — surely — there are a couple of truly extended objects, which have been split into sub-components by Starfinder, but this

is not the only problem. Some very bright point-like objects have been split as well, because the PSF used in Starfinder was cut at a small radius, and the wings/lobes of these bright objects are quite bright. Starfinder actually extracts the lobes of the sources as if they were real individual objects. These cases are corrected along with real extended objects.

The newly-injected objects (i.e. those with SExtractor’s photometry) have IDs starting from 10000 in the PACS blind catalogs.

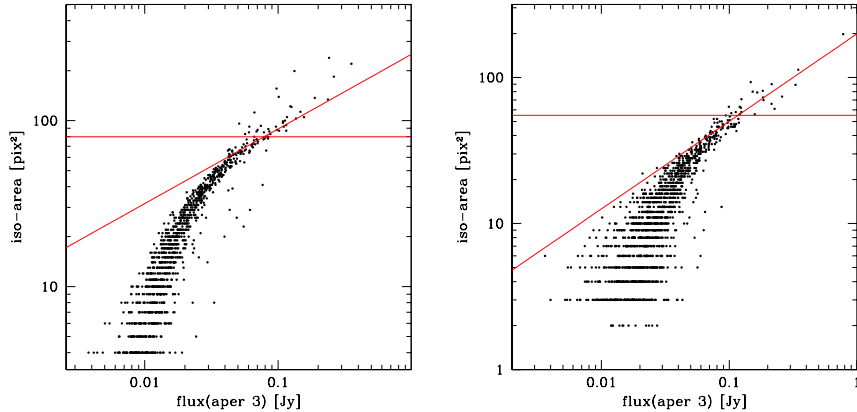


Figure 2: Examples of the criteria adopted to seek for extended/bright sources that might have been split into sub-components by Starfinder (COSMOS 100 μm on the left, 160 μm on the right).

Field/band	A	a	b
COSMOS 100	80	0.45	2.40
COSMOS 160	55	0.60	2.30
ECDFS 100	50	0.80	2.87
ECDFS 160	40	0.80	2.56
EGS 100	60	1.00	3.26
EGS 160	40	0.90	2.70
LH 100	50	0.80	2.90
LH 160	40	0.80	2.58
GOODS-N 100	85	0.63	3.05
GOODS-N 160	70	0.80	3.06
GOODS-S 70	55	0.45	2.56
GOODS-S 100	95	0.45	2.84
GOODS-S 160	70	0.60	2.97

Table 10: Values of parameters A , a and b describing the criteria adopted to fix problems with potential extended sources in PACS maps and catalogs (see Eq. 5), for blank fields.

8.3 Edges of PACS images

The edges of PACS images are rather noisy and a number of spurious sources might have been extracted. We crop the blind catalogs, in order to avoid this problem. For each field, we define 8

Field/band	A	a	b
A1689	75	0.80	3.10
A1689	35	1.00	3.10
A1835	75	0.80	3.05
A1835	35	1.00	3.05
A2218	50	0.80	3.10
A2218	35	1.00	3.05
A2219	75	0.80	3.00
A2219	40	1.00	3.00
A2390	60	0.80	3.00
A2390	35	1.10	3.15
A370	75	1.10	3.55
A370	35	1.00	2.95
CL0024	75	0.80	2.95
CL0024	35	1.00	3.05
MS0451	40	0.80	3.00
MS0451	35	1.00	3.00
MS1054	60	0.80	2.85
MS1054	35	1.00	2.85
MS1358	75	0.80	2.95
MS1358	25	1.00	3.00
RXJ0152	75	1.20	3.55
RXJ0152	35	1.00	2.80
RXJ13475	50	0.80	3.00
RXJ13475	30	1.00	3.05

Table 11: Same as Table 10, but for cluster fields.

points to delimit the perimeter of the trimmed area. Table 13 lists the J2000 coordinates of these 8 corners.

The effective areas covered by the PACS blind catalogs of blank fields are listed in Table 12. The number of blindly-extracted objects listed in Table 8 refers already to these trimmed areas.

Table 12 also includes the extension of the area above half of the maximum depth of each field. This has been computed by convolving coverage maps with the observed PSFs (see Sect. 11.1) and counting all pixels above the threshold $0.5 \times \max(\text{cov}, \text{convolved})$. Values at $100 \mu\text{m}$ and $160 \mu\text{m}$ are comparable, therefore we simply quote the average between the two. GOODS-S represent an exception, since it includes the very deep GOODS-*Herschel* sub-area at 100 and $160 \mu\text{m}$; in this case, the “half-depth area” is measured on the $70 \mu\text{m}$ map only, i.e. refers to PEP data alone.

No trimming of the edges of PACS images has been applied in the case of cluster fields, which show an intrinsically more inhomogeneous coverage and noise due to their small size.

9 Multi-wavelength cross-IDs

The PACS blind catalogs extracted using Starfinder (see Section 8) have been matched to the available $24\mu\text{m}$ source lists by means of a maximum likelihood analysis (Ciliegi et al. 2001; Sutherland & Saunders 1992), taking advantage of the available $24\mu\text{m}$ fluxes.

Field	Effective area	Half-depth [†] area
COSMOS	7182.3524 arcmin ²	7335.6 arcmin ²
ECDFS	1018.2724 arcmin ²	962.1 arcmin ²
EGS	900.4816 arcmin ²	742.6 arcmin ²
LH	687.8832 arcmin ²	592.2 arcmin ²
GOODS-N	272.0344 arcmin ²	201.3 arcmin ²
GOODS-S	238.0104 arcmin ²	202.1 [‡] arcmin ²

[†]: see text.

[‡]: based on 70 μm only.

Table 12: Effective area covered by blank field catalogs, after edge trimming

9.1 Generalities of the likelihood ratio method

The likelihood ratio (LR) technique (Ciliegi et al. 2001; Sutherland & Saunders 1992), is a method for source identification which takes into account the magnitude distribution of the counterparts and the positional errors of both the sample and the counterpart sample.

Here, we briefly describe the formalism. Let

$$p = q(m)f(r)dm dr \quad (6)$$

be the probability that the true MIPS counterpart lies in an infinitesimal box $r \pm dr/2$ and in a magnitude interval $m \pm dm/2$. Where

$$\int_0^\infty f(r)dr = 1 \quad (7)$$

and $f(r)$ is the probability distribution function of the positional errors and $q(m)$ is the expected distribution as a function of magnitude of the counterparts.

The probability for a source to be a background object is given by

$$p_{bck} = n(m)f(r)dm dr, \quad (8)$$

where $n(m)$ is the surface density per magnitude of the background objects.

The likelihood ratio is defined as

$$LR = q(m)f(r)/(n(m)), \quad (9)$$

i.e. the ratio between the probability that the source is the correct identification and the corresponding probability for a background object. Since a PEP source can have more than one MIPS identification, we can calculate the reliability of each individual object. The probability R_i that object i is the correct identification is:

$$R_i = \frac{LR_i}{\sum_j LR_j + (1 - Q)} \quad (10)$$

where the sum is over the set of all candidate counterparts for this particular source and Q is the probability that the MIPS counterpart is brighter than the magnitude limit of the MIPS catalogue.

In order to derive $q(m)$ we count all objects in the MIPS catalogue within a fixed radius r (e.g. 10 arcsec) around each source, defined as $total(m)$. The distribution is then background subtracted and normalized to construct the distribution $q(m)$ of real detections:

Field & Num.	R.A.	Dec.
COSMOS 1	150.7532466	2.9156187
COSMOS 2	149.4967666	2.9156254
COSMOS 3	149.4117188	2.8222615
COSMOS 4	149.4122970	1.6057332
COSMOS 5	149.4756912	1.4941091
COSMOS 6	150.7526407	1.4941120
COSMOS 7	150.8260364	1.6057331
COSMOS 8	150.8266149	2.8222613
ECDFS 1	53.3785641	-27.5383568
ECDFS 2	52.8259634	-27.5382758
ECDFS 3	52.8108601	-27.5615756
ECDFS 4	52.8094166	-28.0632316
ECDFS 5	52.8263598	-28.0832684
ECDFS 6	53.3647384	-28.0833746
ECDFS 7	53.3986771	-28.0583116
ECDFS 8	53.3974186	-27.5616537
EGS 1	215.5847739	53.2084945
EGS 2	215.3652779	53.3240218
EGS 3	215.2651361	53.2997695
EGS 4	214.0772324	52.4585981
EGS 5	214.0852993	52.4343157
EGS 6	214.2927067	52.3274289
EGS 7	214.3884594	52.3514835
EGS 8	215.5794491	53.1905287
LH 1	163.5650432	57.7019121
LH 2	162.8407672	57.7020474
LH 3	162.7682821	57.6575001
LH 4	162.7725515	57.2758446
LH 5	162.7986034	57.2609260
LH 6	163.5123388	57.2610605
LH 7	163.5805542	57.2991948
LH 8	163.5848452	57.6875170
GOODS-N 1	189.3319353	62.4200332
GOODS-N 2	189.2109878	62.4100704
GOODS-N 3	188.8287880	62.1961631
GOODS-N 4	188.8290526	62.1761636
GOODS-N 5	189.1222525	62.0633650
GOODS-N 6	189.2432115	62.0734050
GOODS-N 7	189.6338822	62.2811485
GOODS-N 8	189.6234607	62.3061788
GOODS-S 1	53.1831363	-27.6285765
GOODS-S 2	52.9912176	-27.6618605
GOODS-S 3	52.9799054	-27.6785160
GOODS-S 4	53.0305008	-27.9368914
GOODS-S 5	53.0625501	-27.9752421
GOODS-S 6	53.2625432	-27.9385182
GOODS-S 7	53.2738345	-27.9185064
GOODS-S 8	53.2170348	-27.6718907

Table 13: J2000 coordinates of the 8 points defining the perimeter of the trimmed blind catalogs.

Bands comb.	Number of sources					
	COSMOS	ECDFS	EGS	LH	GOODS-N	GOODS-S
160+100+24	3917	534	466	459	672	783
160+100	3959	584	589	464	757	843
160+24	6023	796	669	697	843	946
100+24	6472	933	837	795	870	980
160	7047	969	940	819	1055	1240
100	7443	1188	1249	973	1040	1189
24 (in PACS trimmed area)	47374	9415	6995	7285	2700	2491
160 (in 24 μm \cap PACS area) ^a	7021	886	754	819	937	1195
100 (in 24 μm \cap PACS area) ^a	7413	1074	1003	973	934	1156
160 100	10531	1572	1600	1328	1338	1586
(160 100)+24	8578	1195	1040	1033	1041	1143

^a: defined as sources having area flag = ‘‘A’’

Table 14: Statistics of maximum-likelihood match in PEP blank fields (in the trimmed PACS area).

$$q(m) = total(m) - n(m)\pi r^2 N_{sources} \quad (11)$$

As a probability distribution of positional errors we adopt a Gaussian distribution with the σ taking into account the combined effect of the source and the identification positional uncertainties.

Once this has been done, a $LR_{threshold}$ value is found in order to maximize the function $(C_{sample} + R_{sample})/2$, where C is the completeness and R the reliability of the sample.

Each PEP source can have more than one MIPS counterpart with LR greater than the $LR_{threshold}$ value. We choose the MIPS counterpart with the highest LR value.

9.2 Application to PEP

The maximum-likelihood method uses a multi-band bands approach, starting from a match between the 160 and 100 μm (and 70 μm when available) catalogs, and then linking the result to 24 μm .

An area flag has been added, assuming value ‘‘N’’ if the given PACS source lies outside of the MIPS 24 μm map, and ‘‘A’’ otherwise.

Cross-IDs are included in the released package. Table 14 summarizes the statistics of the available data. Additional statistics for the PGH GOODS-S field, including 70 μm data, are given in Table 15.

10 Extraction with 24 μm priors

In addition to the blind catalogs extracted with Starfinder, we are also providing a catalog obtained using 24 μm position priors and PSF-fitting. The catalogs of priors used for each blank field are listed in Table 16, and are mostly based on an extraction driven by IRAC source positions.

We warn users that the list of 24 μm priors adopted in the LH field belongs to a preliminary, private catalog, soon to be replaced by an official public release (E. Egami, January 29th 2013, private communication). The PEP DR1 data package includes the file *pep_LH_Xid_old_new_24um.DR1.cat*, providing cross-IDs between our list of priors and the new 24 μm catalog soon to become public.

Bands	GOODS-S
160+100+70+24	348
160+100+70	364
70+24	398
70	462
70 (in $24\ \mu\text{m} \cap \text{PACS area}$)	437
160 100 70	1636
(160 100 70)+24	1157

Table 15: Additional statistics of maximum-likelihood match in PGH GOODS-S, including $70\ \mu\text{m}$ data.

As for clusters, we retrieved $24\ \mu\text{m}$ object lists from different sources. For Abell 2218 we use the $24\ \mu\text{m}$ sources belonging to the PSF-matched internal multi-wavelength catalog produced by S. Berta, G. Grazian and P. Santini with the CONVPHOT (Grazian et al. 2006; de Santis et al. 2007) code. The $24\ \mu\text{m}$ catalogs by Saintonge et al. (2008) were adopted in the case of CL0024, MS0451, and MS1358. For the remainders, we retrieved $24\ \mu\text{m}$ data from the Spitzer archive, reduced them using a standard pipeline, and measured source positions through a quick on the fly extraction with MOPEX.

The catalogs released in PEP DR1 include $24\ \mu\text{m}$ fluxes only for blank fields and for the three clusters covered by Saintonge et al. (2008); in all other cases only positions (and no $24\ \mu\text{m}$ fluxes) are provided. Priors extraction of PACS fluxes is obtained following the method described in Magnelli et al. (2009).

It is worth noting that the MIPS $24\ \mu\text{m}$ catalogs used for GOODS-N and GOODS-S are slightly different from those published by Magnelli et al. (2011), in part due to the use of different IRAC prior catalogs. Nonetheless they have been chosen in order to have homogeneous catalogs with respect to the GOODS-Herschel release (Elbaz et al. 2011).

Tables 17 and 18 summarize the properties of the catalogs extracted with $24\ \mu\text{m}$ priors, for blank and cluster fields respectively.

Users should keep in mind that the error estimate does not take into account confusion noise. We recommend to use any flux below 0.6 mJy in the green band and below 2.0 mJy in the red band with care.

Similarly to blind catalogs, the PACS catalogs extracted with $24\ \mu\text{m}$ priors have been trimmed in order to avoid the edges of images; $24\ \mu\text{m}$ entries lying out of the trimmed area have been entirely excluded from these catalogs. Note, however, that the GOODS-N and ECDFS lists of $24\ \mu\text{m}$ priors cover a smaller area, with respect to the trimming section, therefore the area effectively covered by the prior catalog is smaller than that of the blind catalog. Moreover, in the COSMOS field, although extending beyond the area observed by PACS, the list of priors does not fully cover the N-W and S-E corners of the PACS maps (but the loss in area, with respect to Table 13, is minor).

10.1 Simulations

A total of 10000 artificial sources, split in smaller stints in order to preserve image statistics (see Sect. 8.1), have been added to the PACS science maps, and then extracted with the same configuration used for real objects, with the aim to quantify the detection rate and the fraction of spurious detections in

Field name	24 μm priors list	
	Ref.	3σ Depth
COSMOS	Le Flocc'h et al. (2009)	45 μJy
ECDFS [†]	Magnelli	20–70 μJy
EGS	Magnelli	30 μJy
LH [‡]	Egami (not public)	–
GOODS-N	Magnelli et al. (2011)	20 μJy
GOODS-S	Magnelli et al. (2011)	20 μJy

[†] the 24 μm coverage of ECDFS is highly in-homogeneous

[‡] based on a preliminary version of the 24 μm LH catalog, soon to be superseded (see text).

Table 16: List of 24 μm prior catalogs adopted in prior extraction of PACS catalogs.

the PACS catalogs. We employ the same artificial source lists and simulated images for the “blind” and “priors” catalogs.

The fraction of spurious sources has been derived in two different ways: by blindly extracting from PACS images without any objects (analogous to inverted maps, but obtained by flipping the sign of sub-maps during stacking and hence free of possible artifacts), as well as from simulations (see caption of Fig. 3). The two methods lead to consistent results.

Figure 3 show the results of this analysis in GOODS-N, and Tables 17, 18 include the completeness and spurious fraction values at the 3σ and 5σ levels for all blank and cluster fields, respectively. Curves of the completeness and the fraction of spurious sources as a function of flux are included in the released data package.

Note that — given the inhomogeneity of GOODS-S 100 and 160 μm maps — GOODS-S simulations refer only to the central, deepest area.

10.2 Noise estimate

The extraction with 24 μm priors provides very clean residual maps, which have been used to estimate the r.m.s. noise value of the PEP data. Fluxes through 10000 apertures randomly positioned on the residual maps were extracted. Figure 4 shows the distribution of the extracted fluxes in PGH GOODS-N, peaking around zero, as expected for a well subtracted background, and showing a typical Gaussian profile. Tables 17, 18 report the 1σ noise level thus derived for each field.

11 Flags and additional information

The PACS catalogs included in this first PEP and PGH public release include a series of additional pieces of information, aimed at the best exploitation of the data by all users. The following are included:

- **coverage**, i.e. the actual value of coverage at the location of the given object on PACS maps;
- in blank fields only, the **clean index**, describing if a given PACS object is surrounded by comparably bright (or brighter) sources;

Field & band	S(1σ) mJy	N $S/N \geq 3$	N $S/N \geq 5$	Completeness 3σ	f(spur) 3σ	Completeness 5σ	f(spur) 5σ	S(80%) mJy
COSMOS 100	1.50	8847	3876	0.44	0.09	0.92	0.01	6.35
COSMOS 160	3.27	7620	3068	0.37	0.12	0.86	0.02	14.93
ECDFS 100	1.25	1062	503	0.38	0.10	0.87	0.01	5.60
ECDFS 160	2.61	996	416	0.25	0.28	0.78	0.03	13.70
EGS 100	1.16	1086	517	0.46	0.11	0.90	0.01	5.15
EGS 160	2.46	915	391	0.35	0.23	0.87	0.02	11.02
LH 100	1.24	902	404	0.44	0.12	0.89	0.01	5.40
LH 160	2.92	755	312	0.33	0.20	0.81	0.01	14.30
PGH GN 100	0.31	980	615	0.36	0.10	0.72	0.05	1.97
PGH GN 160	0.68	884	571	0.24	0.32	0.62	0.05	4.56
PGH GS 070	0.27	507	264	0.21	0.24	0.77	0.02	1.39
PGH GS 100	0.17	1112	751	0.21	0.27	0.65	0.05	1.22
PGH GS 160	0.42	989	659	0.18	0.38	0.45	0.14	3.63

Table 17: Statistics of PACS catalogs extracted using position priors at $24\mu\text{m}$, within the trimmed areas. The derivation of the 1σ noise value is described in Sect. 10.2, and is the same as reported for the blind catalog. On the other hand, the catalog has been cut at 3σ and 5σ on the basis of S/N simply computed as Flux/Error for each individual source. Last column reports the flux level at which 80% completeness is reached.

Field & band	S(1σ) mJy	N $S/N \geq 3$	N $S/N \geq 5$	Completeness 3σ	f(spur) 3σ	Completeness 5σ	f(spur) 5σ	S(80%) mJy
PEP A1689 100	0.57	101	69	0.74	0.11	0.87	0.05	2.25
PEP A1689 160	1.38	74	51	0.22	0.25	0.67	0.12	9.05
PEP A1835 100	0.89	66	43	0.48	0.12	0.90	0.03	3.88
PEP A1835 160	2.10	55	34	0.32	0.20	0.75	0.05	11.15
PEP A2218 100	0.71	58	37	0.19	0.18	0.62	0.07	4.47
PEP A2218 160	1.83	46	31	0.44	0.17	0.81	0.11	8.95
PEP A2219 100	0.83	72	50	0.43	0.07	0.86	0.02	3.89
PEP A2219 160	1.98	60	38	0.49	0.09	0.82	0.04	9.45
PEP A2390 100	0.91	112	82	0.50	0.05	0.91	–	3.86
PEP A2390 160	2.54	68	41	0.45	0.10	0.87	0.02	11.10
PEP A370 100	0.90	77	44	0.35	0.13	0.77	0.02	4.73
PEP A370 160	2.28	57	30	0.29	0.13	0.74	0.12	12.72
PEP CL0024 100	0.97	112	70	0.47	0.10	0.90	0.02	4.19
PEP CL0024 160	2.27	95	45	0.28	0.20	0.78	0.03	11.85
PEP MS0451 100	0.86	70	43	0.49	0.11	0.87	0.06	3.73
PEP MS0451 160	2.24	56	30	0.41	0.21	0.85	0.03	10.40
PEP MS1054 100	1.10	107	59	0.42	0.11	0.87	0.01	4.97
PEP MS1054 160	2.57	74	40	0.47	0.12	0.83	0.03	12.85
PEP MS1358 100	0.86	70	37	0.42	0.10	0.85	0.01	4.05
PEP MS1358 160	2.12	52	23	0.42	0.20	0.83	0.01	10.0
PEP RXJ0152 100	1.14	63	33	0.42	0.06	0.86	0.02	5.15
PEP RXJ0152 160	2.55	57	29	0.35	0.17	0.81	0.06	12.54
PEP RXJ13475 100	0.89	45	45	0.43	0.11	0.87	0.02	4.07
PEP RXJ13475 160	2.17	36	36	0.34	0.12	0.79	0.08	10.93

Table 18: Same as Table 17, but for cluster fields.

- in **ECDFS** only, two flags indicating whether a given source is present also in the PGH GOODS-S maps and/or catalogs.

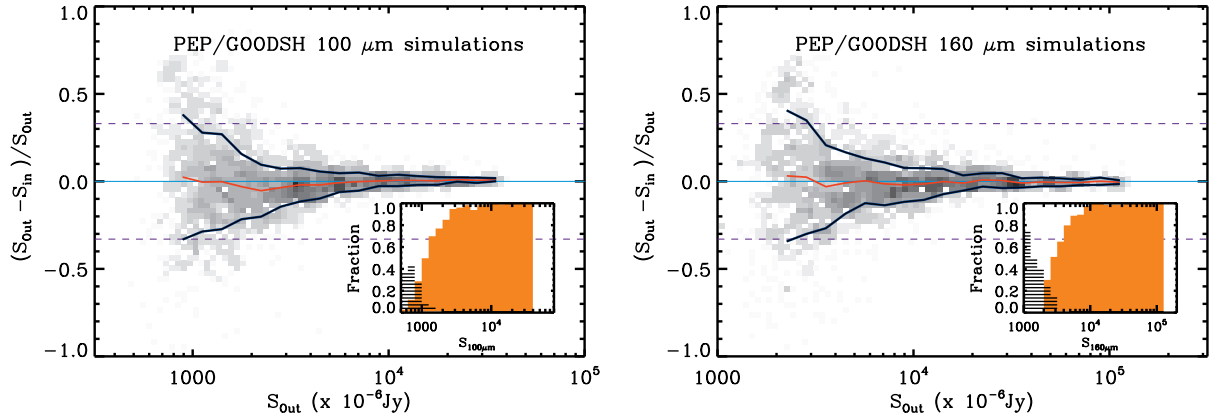


Figure 3: Results of “simulations” in PGH GOODS-N, using $24\mu\text{m}$ position priors. Comparison of input and output fluxes: red lines represent the average photometric accuracy, blue lines set the standard deviation observed in each flux bin (after 3σ clipping). Orange histograms represent the detection rate (or completeness) computed on the artificial injected sources. Completeness is defined as the fraction of sources that have been detected with a photometric accuracy of at least 50% (Papovich et al. 2004). Black hashed histograms show the fraction of spurious sources, defined as sources extracted above 3σ with an input flux lower than $3\sigma(\text{Image})$. The files corresponding to these diagrams, and included in this release are named:

pgh_GOODSN_100um_priors_Err_Compl_Contam.DR1.eps (left),
pgh_GOODSN_160um_priors_Err_Compl_Contam.DR1.eps (right).

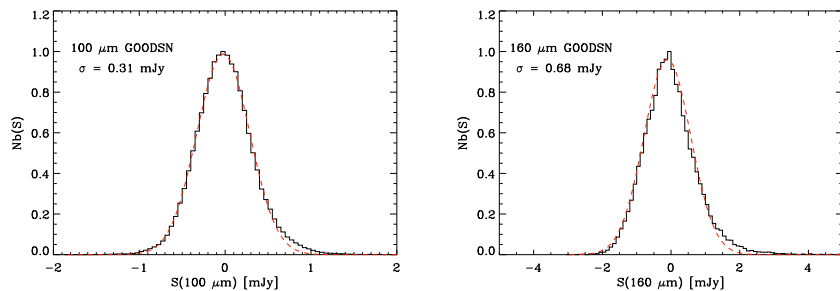


Figure 4: Distribution of fluxes in randomly positioned empty apertures for PGH GOODS-N.

In the following sections, details about each of the above mentioned quantities are provided.

11.1 Coverage value

As previously mentioned, this release includes coverage maps, describing the relative fraction of data contributing to the flux in each map pixel.

We have computed the values of coverage relative to each source in PACS catalogs, by convolving the coverage maps by the PACS observed PSF (specific to each field/band, and normalized to a total power of 1.0) and then reading the resulting value at the position of each object. In this way, an average coverage value, weighted by the profile of the observed PSF is measured. Finally the values extracted from coverage maps have been transformed into equivalent exposures by applying the relation $\text{cov}(s/\text{pix}) = \text{cov} * 0.1/\text{pixfrac}^2 = \text{cov} * 27.78$.

Coverage values for each band are included in blind catalogs, as well as in catalogs extracted with 24 μm priors.

11.2 Clean index

A major source of uncertainty, particularly for the deepest data, comes from the high source density relative to the beam size, i.e., the so-called confusion limit (Condon 1974; Berta et al. 2011). Following the work performed by the GOODS-Herschel team, the source catalogs provided in this data release include an estimator of the purity of the sources, labeled the “clean index”, which was already used in Hwang et al. (2010) and Elbaz et al. (2010, 2011) to identify individual sources with the least probable contamination by bright neighbors. The clean index for a source results from the combination of the number of bright neighbors that it has in each of the Herschel bands observed — i.e., 70, 100 and 160 μm — and in the Spitzer MIPS 24 μm passband. For the purpose of computing the clean index, we define a “bright neighbor” to be a source brighter than half the flux density of the source of interest, and closer than $1.1 \times \text{FWHM}$ of the PSF in each of the Herschel bands. At 24 μm , bright neighbors with $F_{24} > 50\%$ of the central 24 μm source are considered within a distance of 20 arcsec. Simulations confirmed that this configuration represents an efficient reference for the definition of clean areas where sources may be detected with reliable Herschel measurements. At 100 μm and 160 μm , neighbors are considered to lie within 7 and 11 arcsec from each given source. The clean index provided in the catalogs was computed from the numbers of bright neighbors at 24, 100, 160 μm , labeled Neib24, Neib100, Neib160:

$$\text{clean index} = \text{Neib24} + \text{Neib100} \times 10 + \text{Neib160} \times 100 \quad (12)$$

A maximal conservative approach, to avoid the potential effects of neighbors on the photometric accuracy of a given source, would consist into considering only sources with a clean index = 0. However, allowing Neib24 to be ≤ 1 , i.e., accepting at most one bright neighbor at 24 μm within 20 arcsec, provides a relatively robust selection of clean measurements. Elbaz et al. (2011) adopted an intermediate criterion, consisting in requiring $\text{Neib24} \leq 1$ and $\text{Neib}_\lambda \leq 0$ in all Herschel bands. The clean index should be considered here as a flag providing some insight on the purity of the measurements in the Herschel bands for a given source, but not as a strict quality flag that can be used blindly. A forthcoming paper (Leiton et al., in prep.) will discuss this index in more detail. A related approach has been discussed by Brisbin et al. (2010).

The clean index is included only for blank fields, both in catalogs extracted with 24 μm priors, and in cross-ID lists linking blind catalogs to 24 μm data.

11.3 ECDFS additional flags

The area covered by PACS in the ECDFS field actually comprises the entire GOODS-S field, which reaches a much higher depth thanks to the PGH dataset.

Two flags have been computed for the ECDFS field only, describing:

1. if a given PEP ECDFS object is also detected on the PGH GOODS-S maps, and included in PGH catalogs;
2. if a given PEP ECDFS object lies in the area covered by the (trimmed) PGH GOODS-S catalogs.

In the first case, the matching between the ECDFS and GOODS-S catalogs has been performed through a simple closest-neighbor algorithm, adopting a matching radius of 2 arcsec for prior catalogs and of 3 and 4 arcsec for blind 100 and 160 μm catalogs, respectively.

These flags assume a value of 1.0 in case a given ECDFS object is covered by GOODS-S. There do exist cases in which an object detected in ECDFS lies in the GOODS-S area but is not detected in PGH. This happens only for a handful of objects, which have a low S/N ratio (but still above 3σ) in ECDFS, and either disappear or “move” by more than the adopted matching radii when using the deep PGH data.

Both flags flavors are included in all ECDFS PACS catalogs extracted blindly and with 24 μm priors.

12 Comparison between blind and prior catalogs

A direct comparison between our blind catalogs and our catalogs extracted using 24 μm priors is a good test for data self-consistency. Moreover it is useful also as a check for possible mistakes or errors during extraction, calibration, etc.

Figures 5, 6, 7 and 8 presents the comparison between the two flavors of catalogs in COSMOS, ECDFS, EGS, LH; Fig. 9 in GOODS-N, and Fig. 10 in GOODS-S (full catalog). Then, in Fig. 11, we limit the analysis to the central, deepest section of GOODS-S. Figures 12 to 23 present the comparison between the two flavors of catalogs in all cluster fields. For each case, we show:

- the direct comparison of fluxes for sources in common to both catalogs;
- the distribution of unmatched sources in absolute number;
- the distribution of unmatched sources in fraction relative to total in the given flux bin.

Fluxes extracted with the two methods (completely independent, excepted for the adopted PSF profiles) are well consistent to each other.

As far as the distribution of un-matched sources is concerned, we generally find an “excess” of faint objects in the priors catalogs, with respect to the blind one. It is actually expected that the catalogs extracted with 24 μm positional priors are deeper than the blind catalogs and retrieve more faint sources.

Nevertheless, when dealing with deeper and more crowded bands/fields, it turns out that the prior and blind catalogs behave similarly, with a couple of exceptions only. In fact at the faint fluxes, spurious sources and confusion start to play a significant role, and the number of unmatched sources tends to be similar for blind and prior catalogs at all fluxes, ruled by a compromise between reduced instrumental noise, enhanced confusion noise, and enhanced incidence of spurious detections.

A relevant exception exists. In the GOODS-S field (which benefits from the deepest observations available), the blind catalog contains a large number of unmatched objects at fainter fluxes, with respect to the catalog extracted with 24 μm priors. This effect becomes more important when examining the full catalog, while it is partially reduced when limiting to the central, deepest area. We believe that this effect is dominated by spurious detections, which become critical at 160 μm . The blind catalog is overall more affected by this problem, but in the deepest field, this incidence of spurious detections becomes large even in the catalog extracted with 24 μm priors.

In the case of cluster fields, catalogs extracted with 24 μm priors often show a lack of faint sources, with respect to blind catalogs, due to the limited depth of the available 24 μm catalogs.

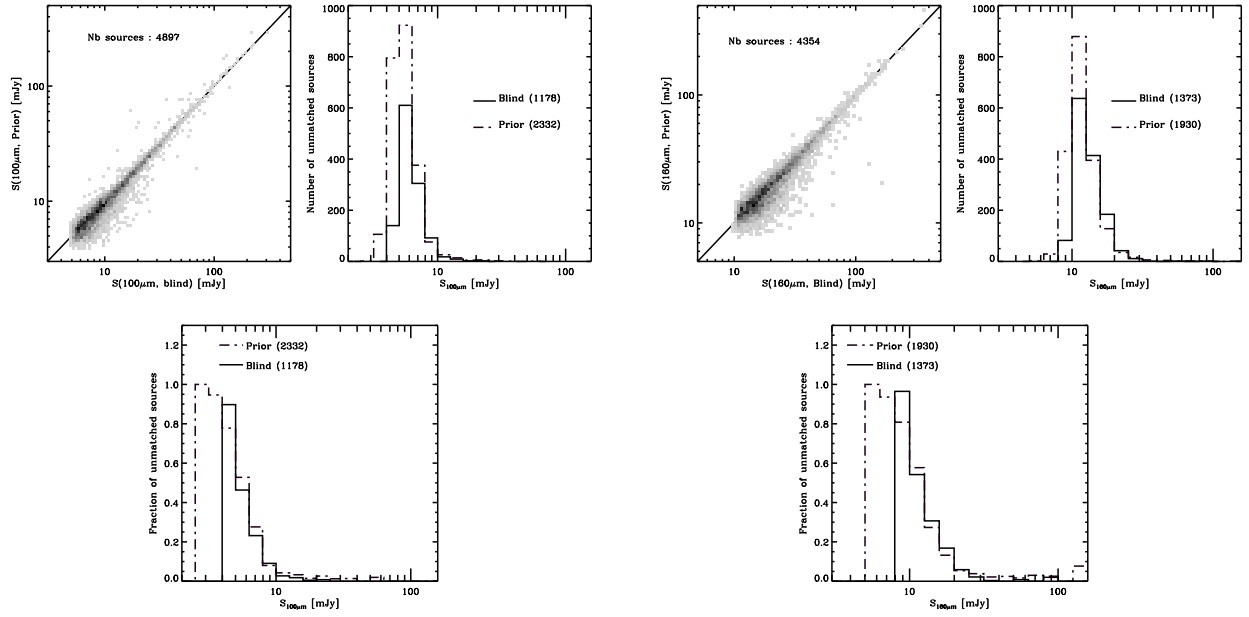


Figure 5: Comparison between blind and priors catalogs in COSMOS.

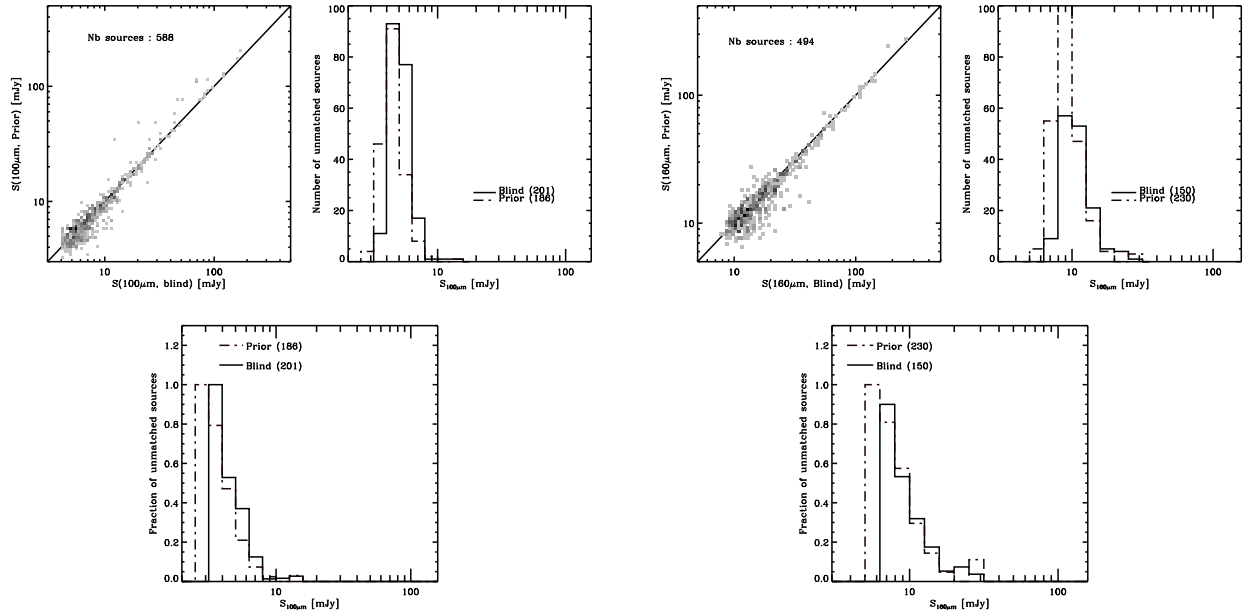


Figure 6: Comparison between blind and priors catalogs in ECDFS.

References

- Berta, S., Magnelli, B., Lutz, D., et al. 2010, A&A, 518, L30
 Berta, S., Magnelli, B., Nordon, R., et al. 2011, A&A, 532, A49
 Bertin, E. & Arnouts, S. 1996, A&AS, 117, 393
 Brisbin, D., Harwit, M., Altieri, B., et al. 2010, MNRAS, 409, 66

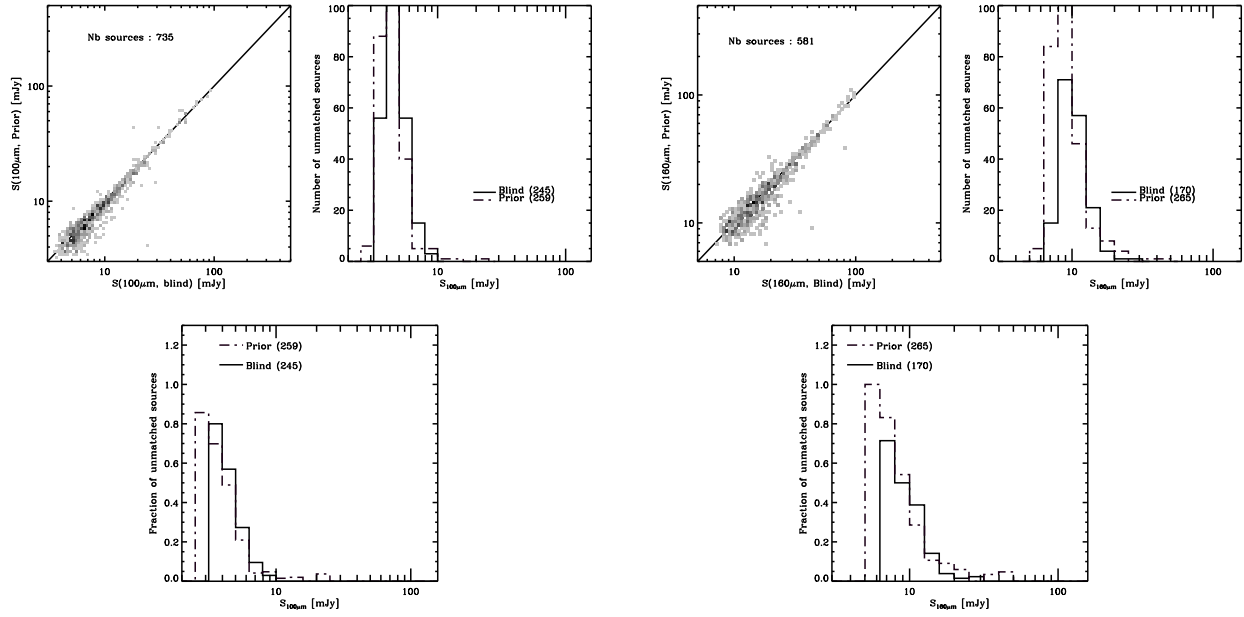


Figure 7: Comparison between blind and priors catalogs in EGS.

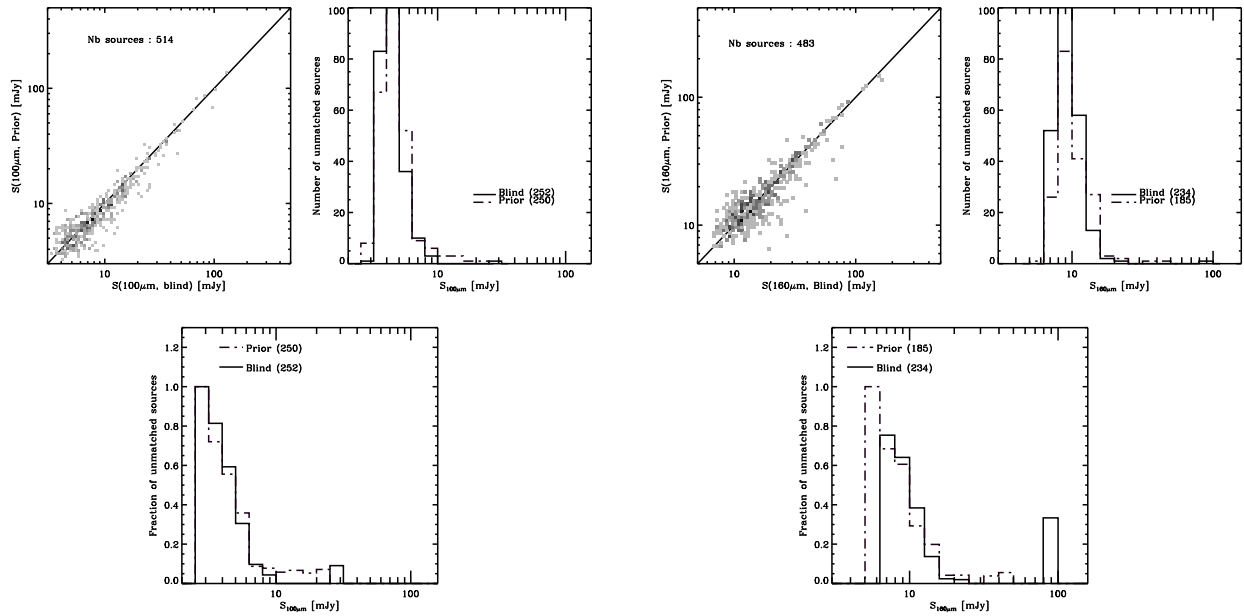


Figure 8: Comparison between blind and priors catalogs in LH.

Ciliegi, P., Gruppioni, C., McMahon, R., & Rowan-Robinson, M. 2001, *Ap&SS*, 276, 957

Condon, J. J. 1974, *ApJ*, 188, 279

de Graauw, T., Helmich, F. P., Phillips, T. G., et al. 2010, *A&A*, 518, L6

de Santis, C., Grazian, A., Fontana, A., & Santini, P. 2007, *New Astronomy*, 12, 271

Diolaiti, E., Bendinelli, O., Bonaccini, D., et al. 2000a, *A&AS*, 147, 335

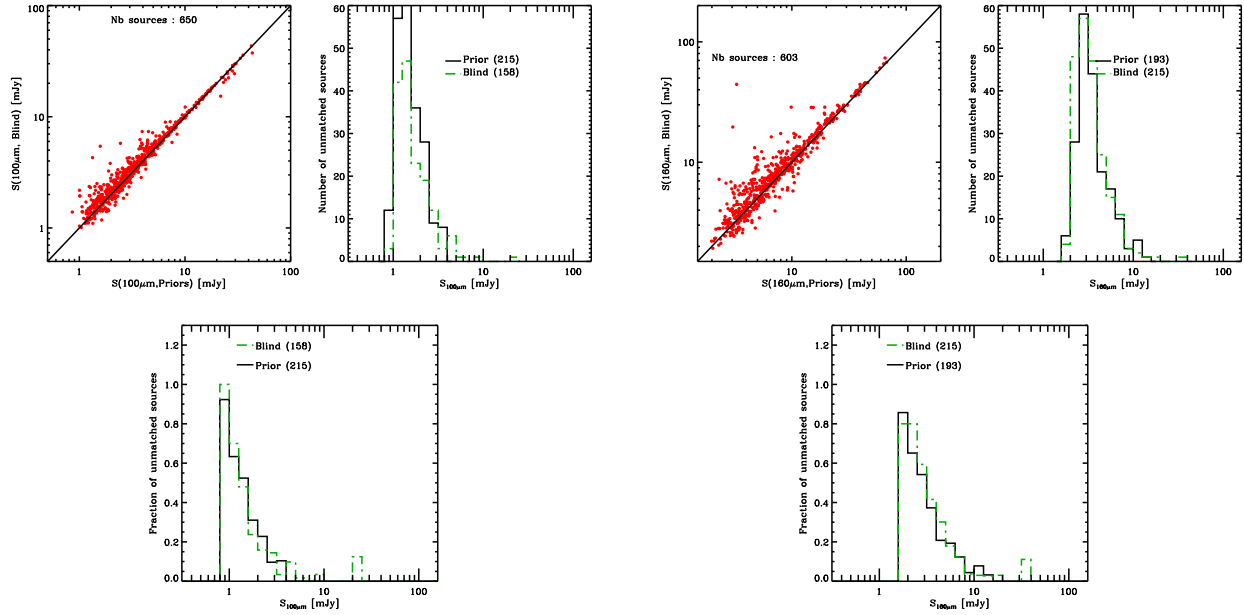


Figure 9: Comparison between blind and priors catalogs in PGH GOODS-N.

Diolaiti, E., Bendinelli, O., Bonaccini, D., et al. 2000b, in Society of Photo-Optical Instrumentation Engineers (SPIE) Conference Series, Vol. 4007, Society of Photo-Optical Instrumentation Engineers (SPIE) Conference Series, ed. P. L. Wizinowich, 879–888

Elbaz, D., Dickinson, M., Hwang, H. S., et al. 2011, *A&A*, 533, A119

Elbaz, D., Hwang, H. S., Magnelli, B., et al. 2010, *A&A*, 518, L29

Fruchter, A. S. & Hook, R. N. 2002, *PASP*, 114, 144

Grazian, A., Fontana, A., de Santis, C., et al. 2006, *A&A*, 449, 951

Griffin, M. J., Abergel, A., Abreu, A., et al. 2010, *A&A*, 518, L3+

Hwang, H. S., Elbaz, D., Magdis, G., et al. 2010, *MNRAS*, 409, 75

Le Floc'h, E., Aussel, H., Ilbert, O., et al. 2009, *ApJ*, 703, 222

Lutz, D., Poglitsch, A., Altieri, B., et al. 2011, *A&A*, 532, A90

Magnelli, B., Elbaz, D., Chary, R. R., et al. 2009, *A&A*, 496, 57

Magnelli, B., Elbaz, D., Chary, R. R., et al. 2011, *A&A*, 528, A35

Magnelli, B., et al. 2013, in preparation

Oliver, S., Frost, M., Farrah, D., et al. 2010a, *MNRAS*, 405, 2279

Oliver, S. J., Wang, L., Smith, A. J., et al. 2010b, *A&A*, 518, L21+

Papovich, C., Dole, H., Egami, E., et al. 2004, *ApJS*, 154, 70

Pilbratt, G. L., Riedinger, J. R., Passvogel, T., et al. 2010, *A&A*, 518, L1+

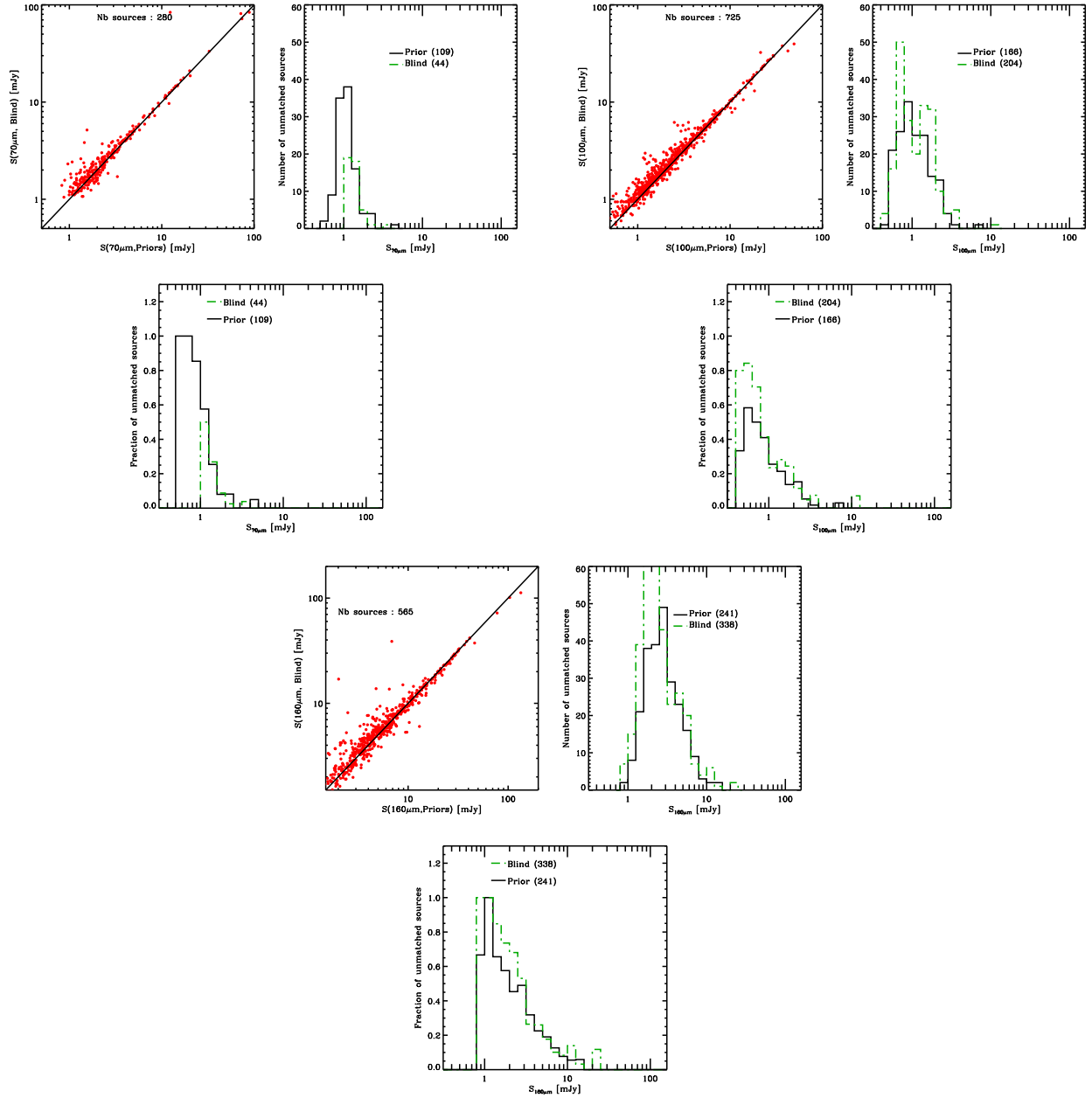


Figure 10: Comparison between blind and priors catalogs in PGH GOODS-S.

Poglitsch, A., Waelkens, C., Geis, N., et al. 2010, *A&A*, 518, L2+

Popesso, P., Magnelli, B., Buttiglione, S., et al. 2012, *ArXiv:1211.4257*

Saintonge, A., Tran, K.-V. H., & Holden, B. P. 2008, *ApJ*, 685, L113

Smith, G. P., Haines, C. P., Pereira, M. J., et al. 2010, *A&A*, 518, L18

Starck, J.-L. & Murtagh, F. 1998, *PASP*, 110, 193

Sutherland, W. & Saunders, W. 1992, *MNRAS*, 259, 413

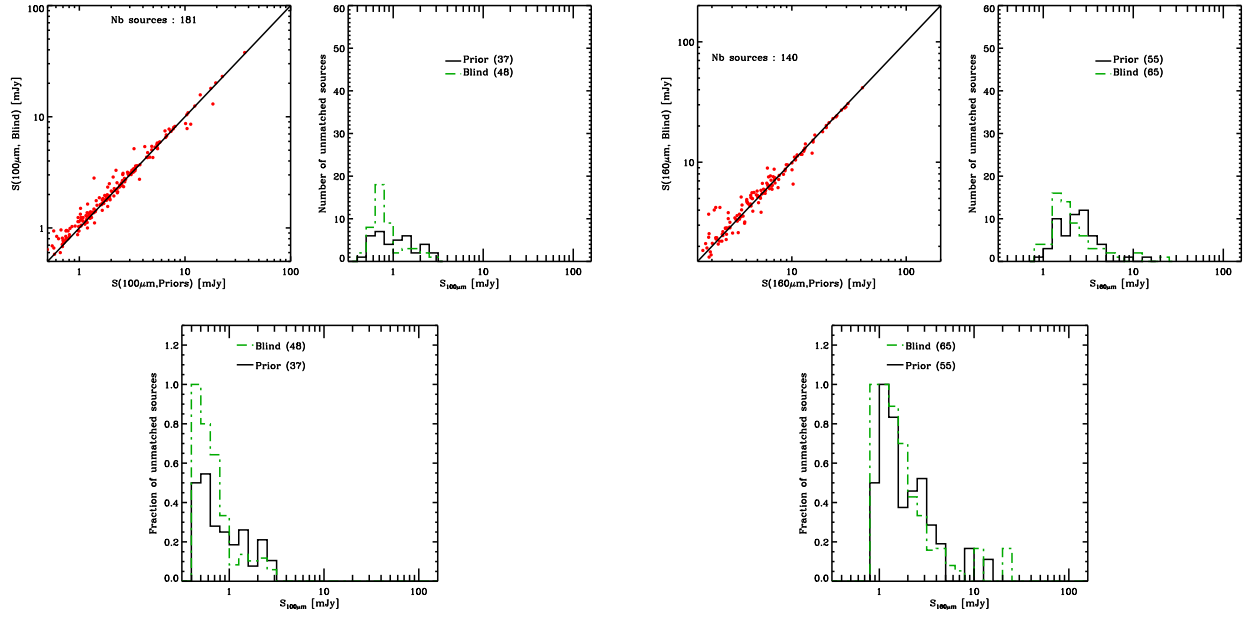


Figure 11: Comparison between blind and priors catalogs in PGH GOODS-S, limited to the central, deepest area.

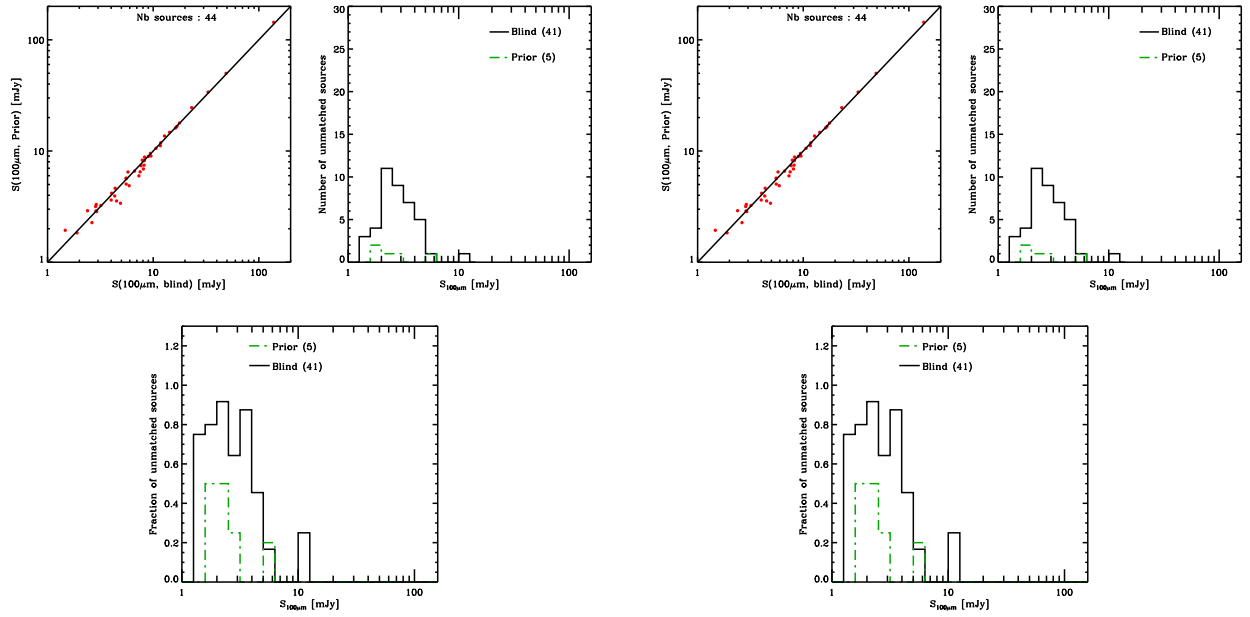


Figure 12: Comparison between blind and priors catalogs in A1689.

Wieprecht, E., Schreiber, J., de Jong, J., et al. 2009, in *Astronomical Society of the Pacific Conference Series*, Vol. 411, *Astronomical Data Analysis Software and Systems XVIII*, ed. D. A. Bohlender, D. Durand, & P. Dowler, 531

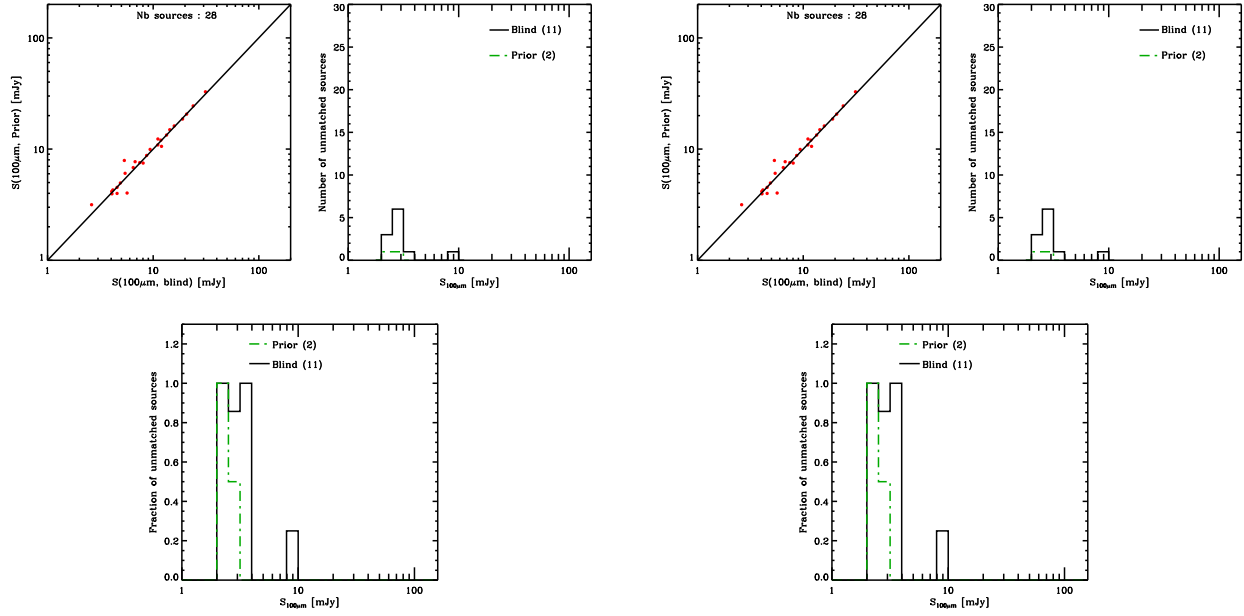


Figure 13: Comparison between blind and priors catalogs in A1835.

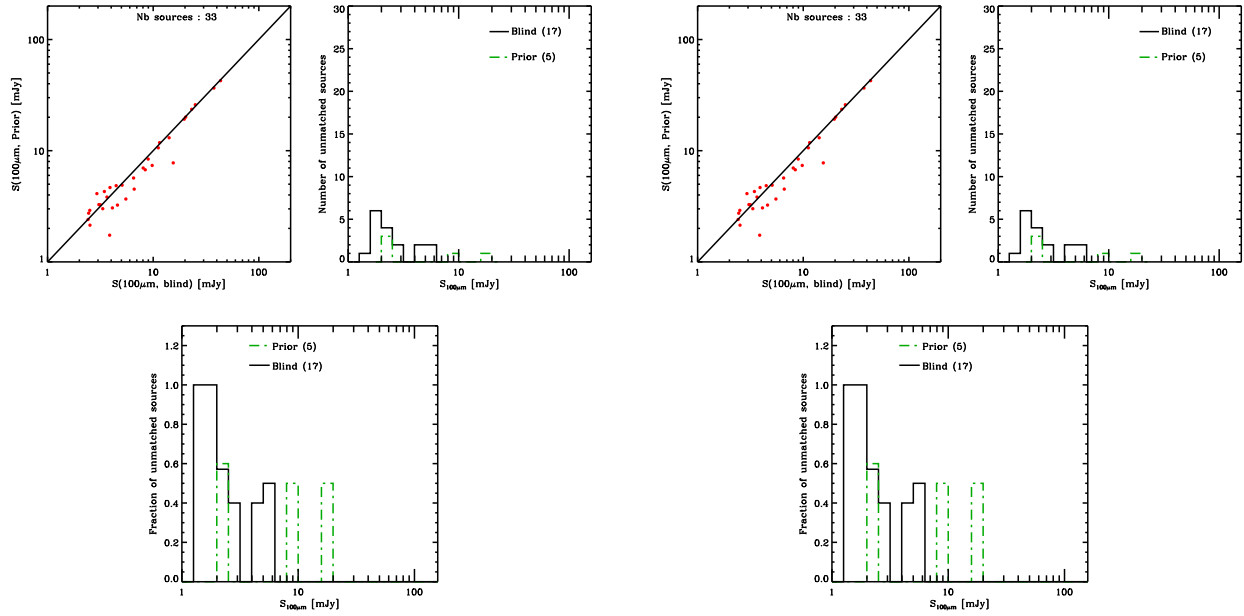


Figure 14: Comparison between blind and priors catalogs in A2218.

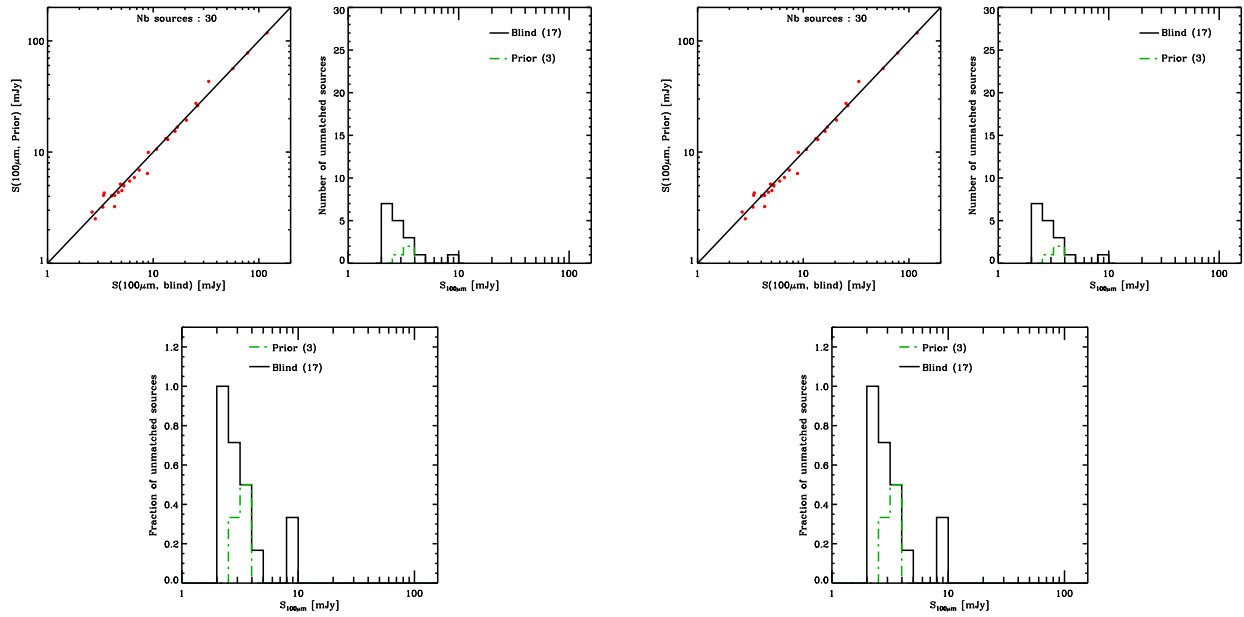


Figure 15: Comparison between blind and priors catalogs in A2219.

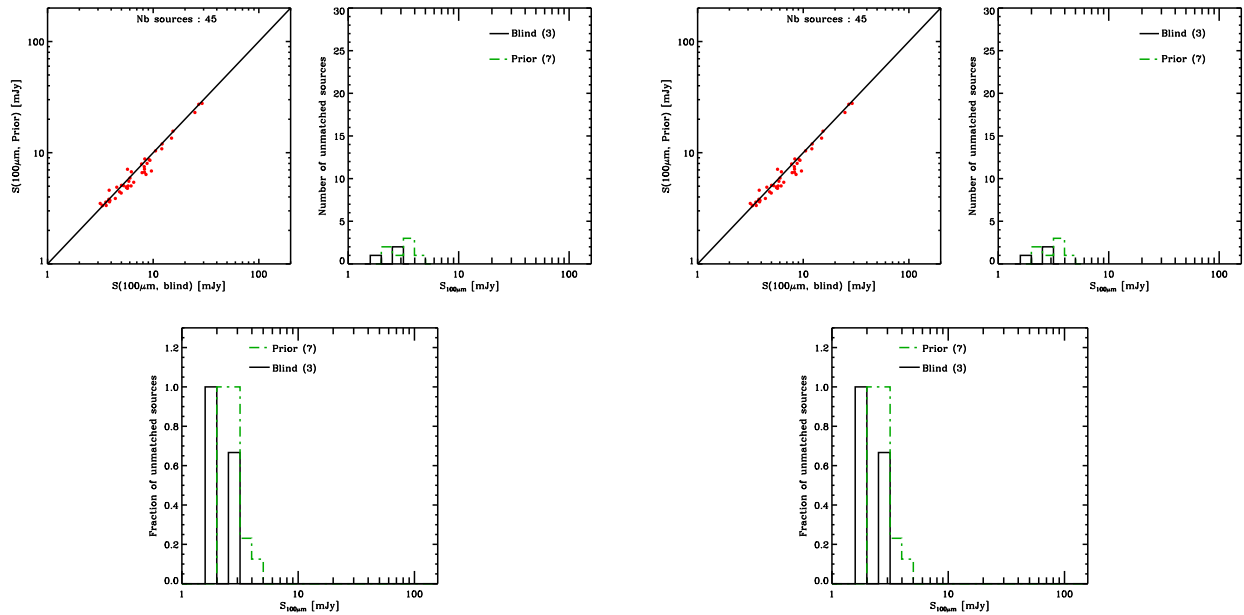


Figure 16: Comparison between blind and priors catalogs in A2390.

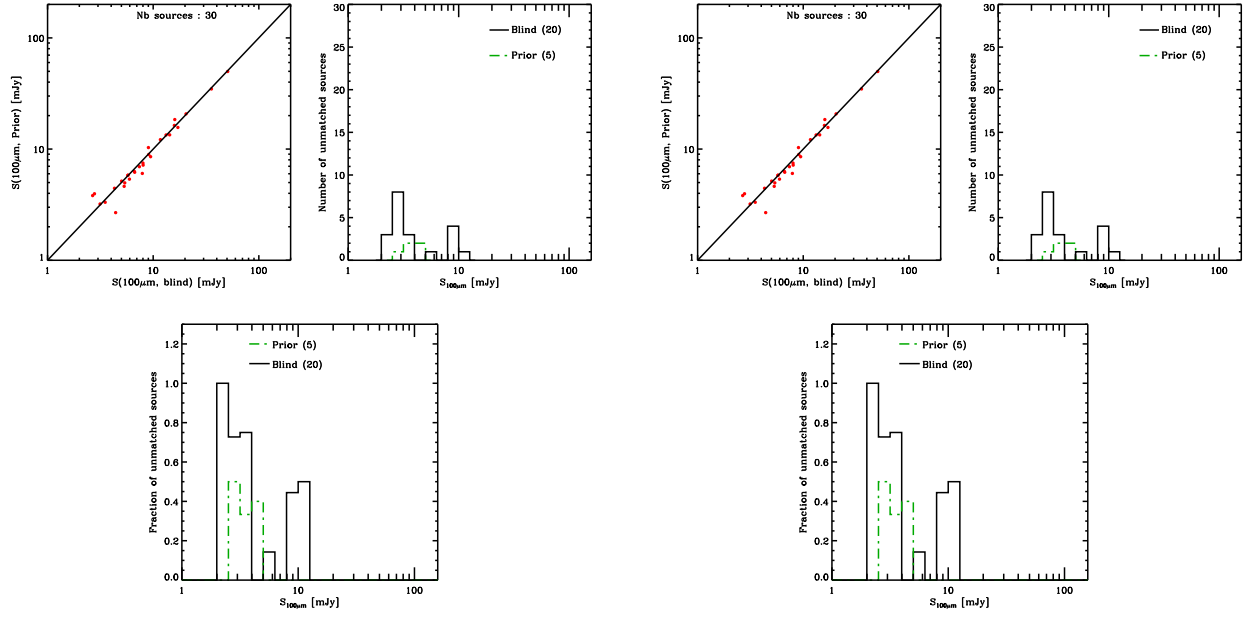


Figure 17: Comparison between blind and priors catalogs in A370.

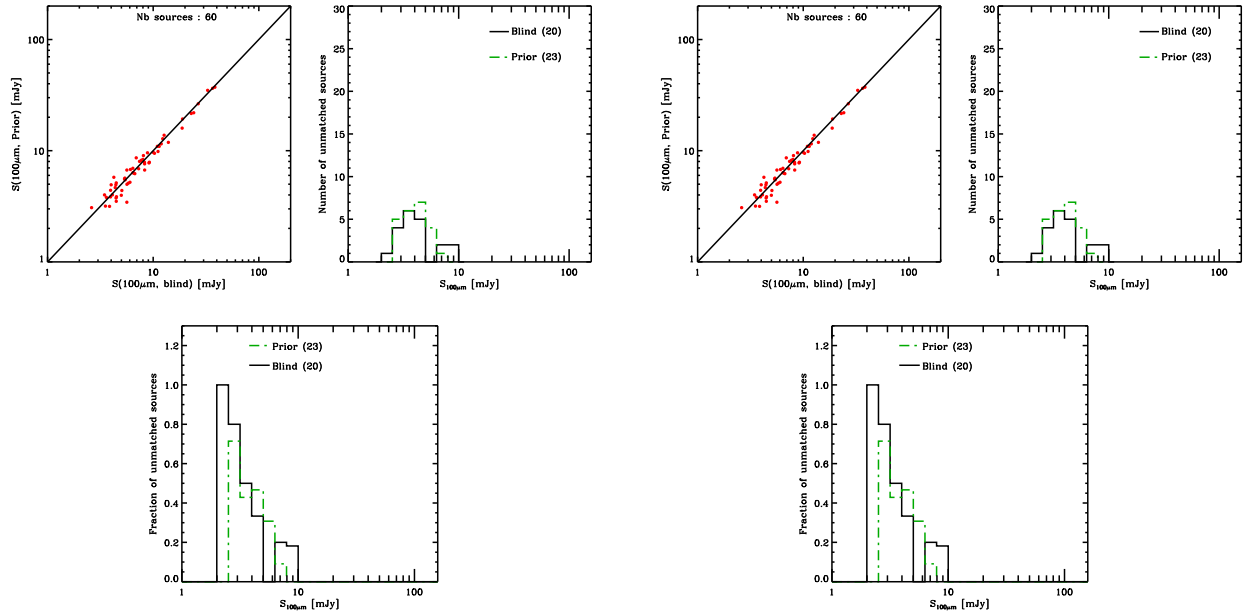


Figure 18: Comparison between blind and priors catalogs in CL0024.

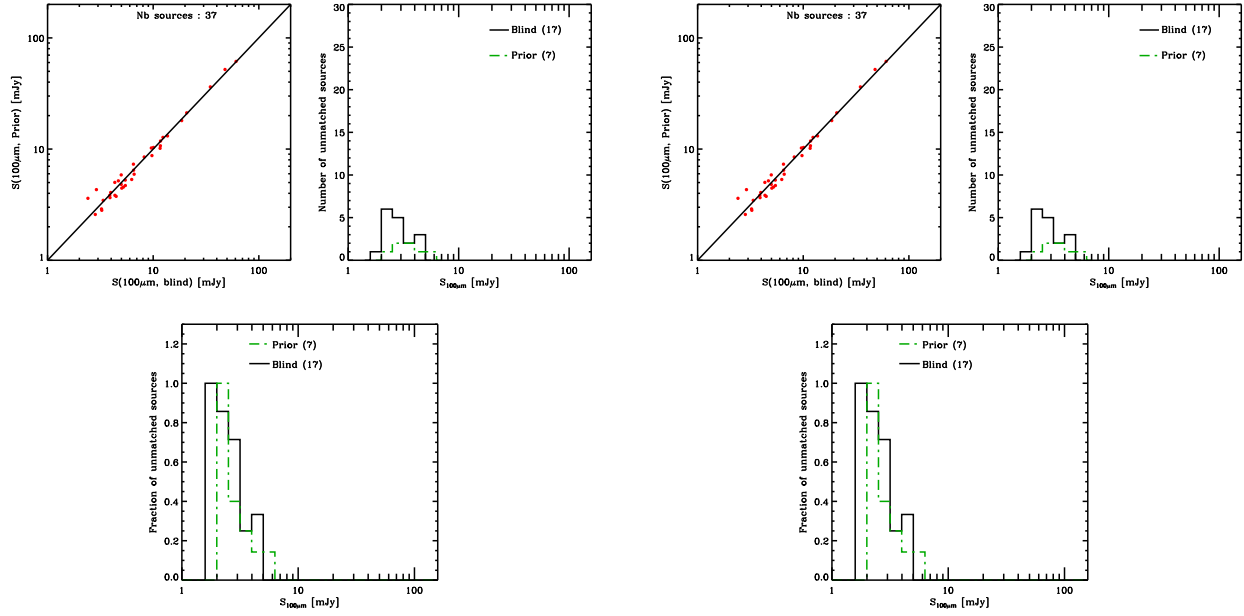


Figure 19: Comparison between blind and priors catalogs in MS0451.

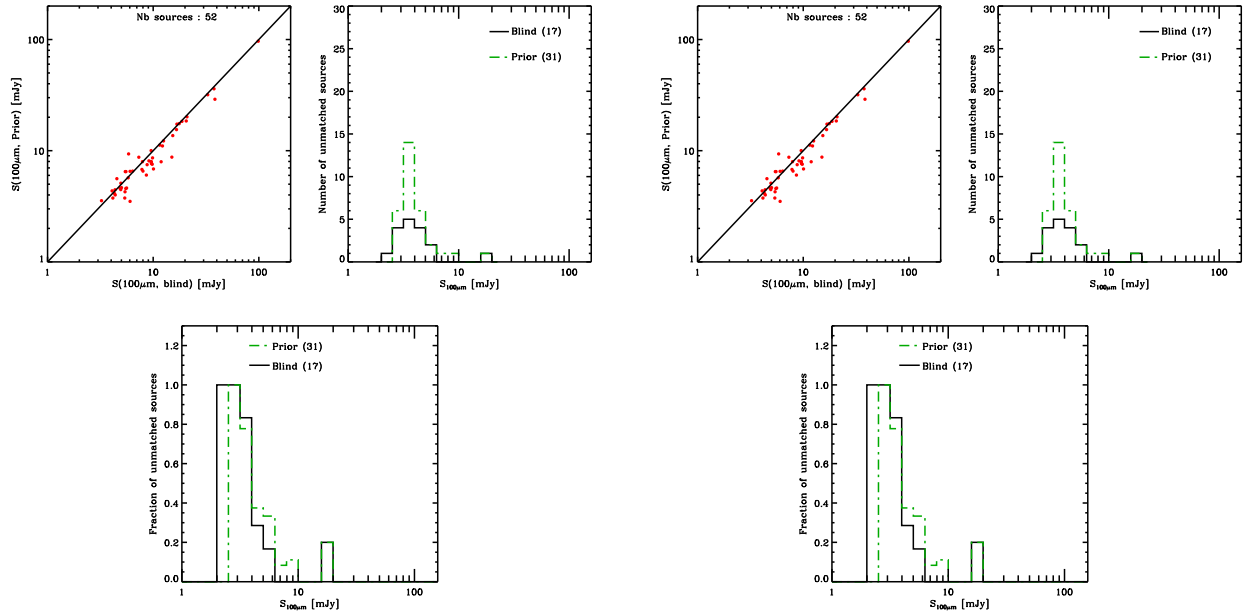


Figure 20: Comparison between blind and priors catalogs in MS1054.

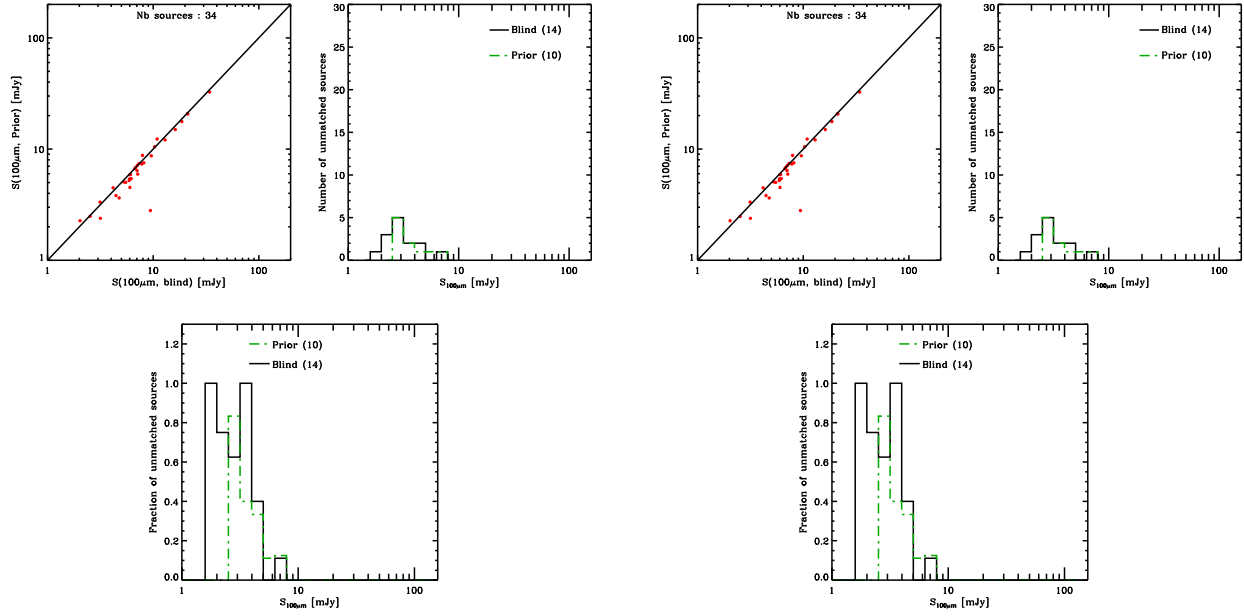


Figure 21: Comparison between blind and priors catalogs in MS1358.

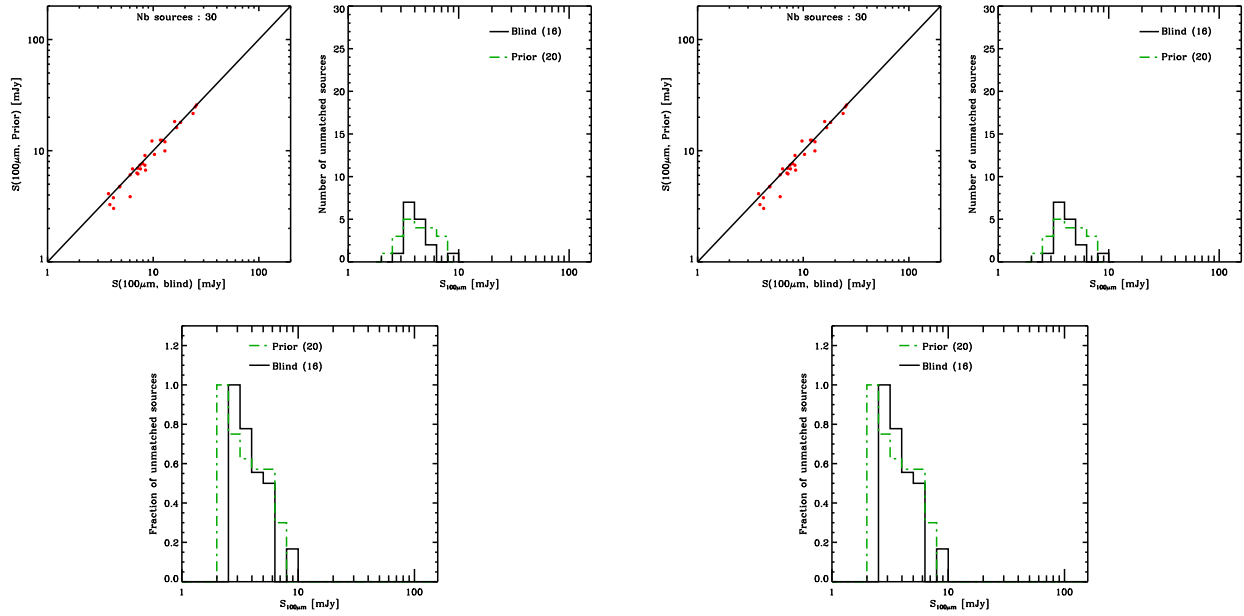


Figure 22: Comparison between blind and priors catalogs in RXJ0152.

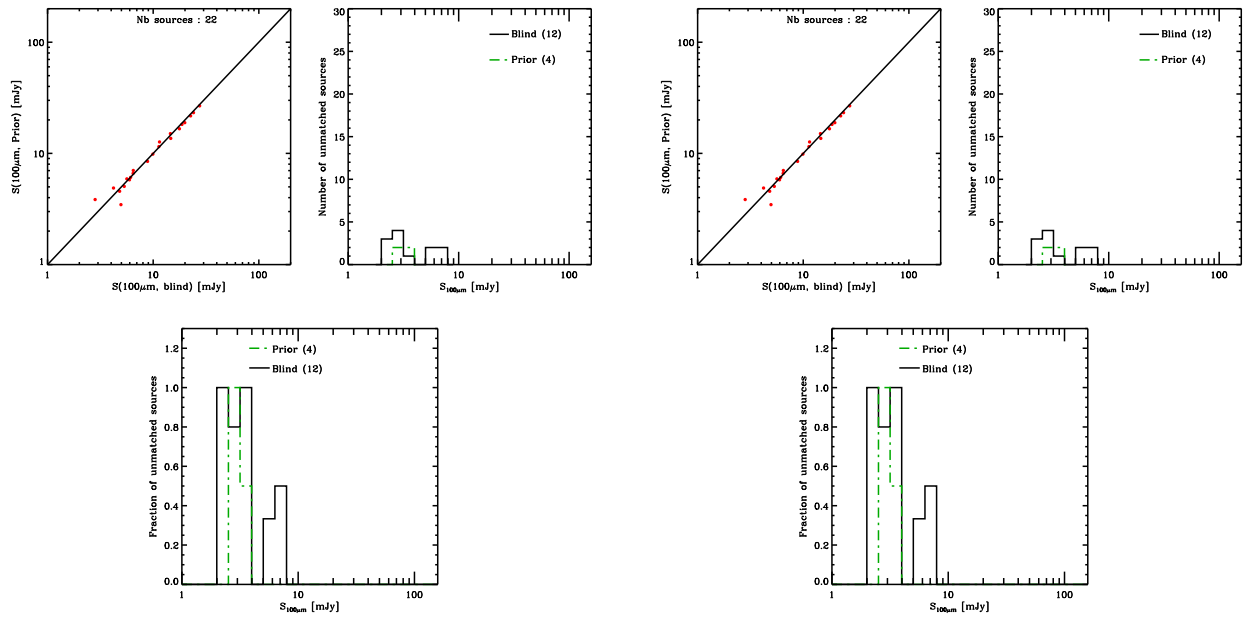


Figure 23: Comparison between blind and priors catalogs in RXJ13475.